UNIVERSITY OF OKLAHOMA

GRADUATE COLLEGE

GEOPHYSICAL INVESTIGATION OF IRON-SULFUR REDOX DYNAMICS IN SULFIDIC SOILS: A CASE STUDY FROM ZODLETONE SPRING, OKLAHOMA

A THESIS

SUBMITTED TO THE GRADUATE FACULTY

in partial fulfillment of the requirements for the

Degree of

MASTER OF SCIENCE

By DANI STORMS

Norman, Oklahoma

2025

GEOPHYSICAL INVESTIGATION OF IRON-SULFUR REDOX DYNAMICS IN SULFIDIC SOILS: A CASE STUDY FROM ZODLETONE SPRING, OKLAHOMA

A THESIS APPROVED FOR THE

SCHOOL OF GEOSCIENCES

BY THE COMMITTEE CONSISTING OF

Dr. Caitlin Hodges, Chair

Dr. Shannon Dulin

Dr. Joseph Panzik

Acknowledgements

This project would not have been possible without the expertise and guidance of Dr. Caitlin Hodges, to whom I am deeply grateful. Additionally, I appreciate Dr. Andrew Elwood Madden for his contributions and time dedicated to this project. I am also thankful for my committee members, Dr. Joseph Panzik and Dr. Shannon Dulin, for their feedback and knowledge they have shared with me. I am particularly thankful to my first geology professor, Dr. Sarah Sheffield, who unknowingly changed the course of my life.

Thank you to my mentors and colleagues who have supported and encouraged my growth as a researcher, and person. In a time of uncertainty, it has been an honor to work alongside those committed to fostering inclusion, education, and advocacy for the scientific community.

I could not have completed this without the unconditional support and love of my wife, Cresencia Storms, and our dog, Zion. Words cannot express my gratitude to my dad, Michael Storms, whose hard work and sacrifices made it possible for me to build something meaningful of my own. I also appreciate my siblings, Tearsa, Nick, and Collin for their constant support and thank my family-in-law for their confidence in me. This accomplishment would not have been possible without the endless encouragement from my family and friends.

A special thank you and dedication is owed to my grandpa, Ed “Papa” Storms, for instilling the philosophy that there will always be more to learn. Finally, I wish to recognize those who are resting in peace and unable to witness this achievement, but whose love and presence continue to shape me. Most of all, my mom, Robin Storms. I carry your presence and strength into every milestone.

TABLE OF CONTENTS

LIST OF TABLES

LIST OF FIGURES

Abstract

This study investigates subsurface iron-sulfur redox dynamics in anaerobic acidic sulfate soils at Zodletone Spring in southwest Oklahoma by integrating noninvasive geophysical method electromagnetic induction (EMI) and Indicator of Reduction In Soil (IRIS) devices. EMI was used to collect apparent electrical conductivity (ECa), which was processed through inversion modeling to better estimate true electrical conductivity (EC) and generate a three-dimensional model of the subsurface. Slices of the model revealed distinct redox transitions between 0.4-0.6m across majority of the study area. IRIS devices confirmed strongly reducing conditions through the removal of iron oxide paint (FeOOH) and precipitation of iron monosulfides (FeS). A statistically positive correlation was observed between elevated EC and FeS coverage ($R^2 = 0.52$, $p = 0.008$), while remaining FeOOH showed a negative correlation with EC ($R^2 = 0.59$, $p = 0.003$), supporting the use of EMI as a noninvasive proxy for monitoring redox activity. These findings demonstrate the value of EMI for identifying redox transition zones in acidic sulfate soils, with important implications for monitoring acidification through oxidation and supporting wetland remediation. The findings also suggest broader relevance for planetary exploration, where subsurface iron-sulfur cycling in low oxygen environments may serve as a biosignature of microbial habitability.

Chapter 1: Introduction

1.0 Motivation

1.0.1 Iron-Sulfur World Hypothesis

Early life on Earth likely emerged within deep ocean hydrothermal vent systems which are dynamic environments defined by geochemical gradients where hot, alkaline, mineral-rich fluids interact with the cooler, acidic, iron-rich waters of the Hadean Ocean (Russel et al., 1994; Schröder et al., 2016). The sharp contrasts in temperature, pH, and oxidation-reduction (redox) potential created highly reactive chemical gradients that likely drove the precipitation of iron-sulfide minerals, forming bubble-like structures known as "probotryoids" (Russel et al., 1994). These membranes isolated and concentrated organic molecules by adsorption, protecting them from dilution and oxidation (Russel et al., 1994). The abundance of hydrogen sulfide (H_2S) and hydrogen gas (H_2) at these sites intensified the redox gradients, creating strongly reducing conditions (Russel et al., 1994; Schröder et al., 2016). These conditions facilitated the chemical transformation of oxidized inorganic carbon sources, such as carbon monoxide (CO) and carbon dioxide (CO_2), into increasingly more complex organic molecules (Russel et al., 1994; Schröder et al., 2016; Wächtershäuser, 1992). The persistent and steep redox gradients across mineral-rich pyritizing mounds served as catalytic reactors which stabilize the synthesized organics and enable early metabolic pathways (Camprubi et al., 2017; Russel et al., 1994).

Wächtershäuser's (1992) iron-sulfur world hypothesis specifically highlights the critical role of these redox gradients, suggesting that early autotrophic organisms required a coupling mechanism to overcome the kinetic barriers. He proposed the "pyrite-pulling" mechanism, wherein the oxidation of iron sulfide (FeS) to pyrite (FeS_2) provided an energetically favorable

redox reaction directly coupled to, and enabling the reduction of CO_2 into organic compounds using H_2 as the electron donor (Camprubi et al., 2017; Wächtershäuser, 1992). This mineral-driven redox coupling significantly reduced the kinetic barriers, allowing for the bridging of inorganic geochemical processes to the earliest biochemical reactions. Therefore, these environments can be considered analogous to early Earth, as they support microbial communities such as purple and green sulfur bacteria. These organisms closely resemble the dominant life forms in Earth's anoxic oceans for nearly a billion years and are still found today in extreme, sulfide-rich environments (Johnston et al., 2009).

Iron sulfide minerals continue to influence modern biogeochemical cycling through their roles in nutrient dynamics and carbon fixation processes, driven fundamentally by redox reactions (Camprubi et al., 2017; Schröder et al., 2016; Wächtershäuser, 1992). The geological record provides evidence of past redox shifts through Banded Iron Formations (BIFs), which document the global transition from early iron-based metabolisms to oxygenic photosynthesis following the Great Oxidation Event (Schröder et al., 2016). Iron redox reactions are also central to astrobiological investigations for planetary habitability. Extensive iron carbonate deposits formed during Mars' Noachian eon suggest that Mars experienced active redox cycling, analogous to processes that facilitated early life on Earth (Schröder et al., 2016). These deposits emphasize the importance of redox gradients as potential universal prerequisites for habitability and illustrate the parallels between Earth's early biogeochemical evolution and potential habitable conditions in extraterrestrial environments.

1.0.2 Iron and Sulfur on Mars

Iron and sulfur exist in multiple oxidation states (e.g., Fe^{2+}/Fe^{3+} and S^{2-} to S^{6+}), and transitions between reduced and oxidized forms significantly influence planetary habitability (Wong et al.,

2021). On Mars, these redox processes offer insights into the planet's environmental evolution, including past water activity and potential conditions that could support microbial life. The Curiosity rover began its mission in August 2012 with the purpose of searching for indicators of ancient habitable environments on Mars, which include redox sensitive elements such as sulfur and iron (Rampe et al., 2020).

Sulfur has been detected in abundance in Martain surface minerals, predominantly in the oxidized sulfate forms of gypsum and jarosite which indicate water-driven geochemical alterations (McAdam et al., 2022; Wong et al., 2021). However, reduced sulfide phases are also observed and provide evidence of complex redox interactions and potential microbial energy sources (McAdam et al., 2022; Wong et al., 2021). Iron appears similarly as predominantly oxidized Fe^{3+} minerals such as hematite and goethite, although reduced Fe^{2+} phases are also present, suggesting fluctuations between oxidizing and reducing environments (McAdam et al., 2022; Wong et al., 2021).

These redox processes involving sulfur and iron result in distinct mineral assemblages that significantly influence soil electrical conductivity. By mapping variations in conductivity, it is possible to identify redox interfaces in the subsurface, where transitions between oxidation and reduction occur, and serve as critical locations for studying geochemical cycling. Geophysical techniques such as electromagnetic induction (EMI) can complement geochemical analyses by providing valuable insights into subsurface redox gradients, evaluating potential microbial energy sources, and identifying zones favorable for biosignature preservation. Mounting an EMI sensor on a future Mars rover would offer a powerful, non-invasive tool to probe below the surface, enabling the detection of hidden redox boundaries that are inaccessible to surface-based instruments alone. Such an addition would significantly enhance our ability to locate and

interpret past habitable environments and guide targeted sampling for astrobiological investigation.

1.1 Soil

1.1.1 Introduction to Hydric Soils and Indication of Reduction In Soil (IRIS) Devices

The Soil Conservation Service (1994) defines hydric soils in the United States as "soils that formed under conditions of saturation, flooding, or ponding long enough during the growing season to develop anaerobic conditions in the upper part." Anaerobic environments develop when prolonged saturation restricts oxygen diffusion and microbial activity depletes the available oxygen supply (Berkowitz et al., 2021). Without available O_2, microbial decomposition considerably decreases and can lead to an accumulation of organic matter (USDA-NRCS, 2024; Vaughan et al., 2016).

To continue respiration and decomposition in the absence of oxygen, microbes resort to reducing alternate, less thermodynamically favorable compounds such as nitrate (NO_3^-), sulfate (SO_4^{2-}), and ferric iron (Fe^{3+}), which are known as terminal electron acceptors (TEAs) (Castenson & Rabenhorst, 2006; Duball et al., 2022; Jenkinson & Franzmeier, 2006). Reduction can also occur abiotically as Fe^{3+} can be reduced to Fe^{2+} by electron donors such as hydrogen gas (H_2) or hydrogen sulfide (H_2S). These processes allow for the translocation and reduction of Fe and S and accumulation of organic matter to be key morphological features of hydric soils (USDA-NRCS, 2024; Vaughan et al., 2016). Since these morphologies reflect prolonged or repetitive saturation, it makes them effective indicators for wetland classification (Rabenhorst & Burch, 2006; USDA-NRCS, 2024). These features, shaped by anaerobic conditions, remain consistent

despite seasonal hydrologic variations, underscoring their diagnostic value (USDA-NRCS, 2024).

Indicator of Reduction In Soil (IRIS) devices (or films) are used for assessing redox processes and redox potential in hydric soils. They were originally introduced by Jenkinson (2002) with the idea that a naturally occurring, colored mineral, such as an iron oxide, will visibly dissolve when exposed to reducing conditions. IRIS devices utilize synthetic Fe oxides painted onto polyvinyl chloride (PVC) tubes or film strips. Removal of the Fe oxide 'paint' serves as a proxy for reduction in anaerobic environments (Castenson & Rabenhorst, 2006; Jenkinson & Franzmeier, 2006; Rabenhorst et al., 2010). The method can provide an economically sustainable method of documenting reduction in hydric soils. Although FeOOH is technically an iron oxyhydroxide, for the purpose of this text, the iron oxide paint in reference to IRIS devices will be referred to interchangeably as FeOOH or iron oxide for simplicity.

Researchers conducted a range of method development steps and trials to determine the most effective procedure of constructing IRIS devices (Jenkinson & Franzmeier, 2006). Ultimately, Rabenhorst and Burch (2006) determined that a mix of ferrihydrite (FH) and approximately 30-40% goethite to maintain a balance between high reactivity and good adhesion. FH is a more favorable iron oxide due to having a lower redox potential (Eh) which allows it to undergo reductive dissolution before more crystalline Fe oxides such as goethite and hematite (Rabenhorst & Burch, 2006). However, goethite is a necessary addition to ensure durability and proper adhesion to the tubes (Rabenhorst & Burch, 2006). Ferrihydrite also may better represent Fe oxides that form in wetland environments that experience alternating reduction and oxidation processes (Rabenhorst & Burch, 2006). This is supported by laboratory testing by Schwertmann

& Taylor (1989) and equilibrium reactions of amorphous Fe oxides documented in Lindsay (1979).

Fundamentally, a relationship exists between the quantity of FeOOH paint removal and the redox potential of the soil (Castenson & Rabenhorst, 2006; Jenkinson & Franzmeier, 2006). In saturated, anaerobic horizons which typically have a lower Eh, some to all FeOOH coating is expected to be removed, while soil that is moist but not fully saturated is expected to have minor removal over a duration of two weeks (Jenkinson & Franzmeier, 2006). However, if the system is very strongly reducing, the reduction of sulfate to sulfide can occur and allow for the formation of iron monosulfides (Duball et al., 2022).

1.1.2 IRIS Devices in Sulfidic Soils

A series of redox reactions involving iron and sulfur species can be observed through visual changes on the IRIS devices. In anaerobic environments, Fe^{3+} can be reduced to its more soluble form of Fe^{2+} by electron donors such as hydrogen gas (H_2) or hydrogen sulfide (H_2S) (Duball et al., 2020; Mebel & Hwang, 2001; Yao & Millero, 1996). Once reduced, Fe^{2+} can react with available sulfides and facilitate the precipitation of iron monosulfides (FeS) (Duball et al., 2020).

These FeS precipitates appear as black to dark gray coatings on the IRIS devices and help identify zones of active iron-sulfur redox cycling (Berkowitz et al., 2019; Duball et al., 2022; Vaughan et al., 2016). However, iron sulfide minerals are unstable and may be oxidized upon exposure, resulting in the generation of sulfuric acid and contributing to local acidity (Berkowitz et al., 2019; Fanning et al., 1989; Wessel & Rabenhorst, 2017). Due to the destruction of FeS when oxidized, IRIS films should be immediately documented after being removed from the soil. The half and full reactions of these processes are summarized in **Table 1**.

Process	Half reactions	Full reaction
Reduction of Fe^{3+} to Fe^{2+}	$Fe^{3+} + e^- \rightarrow Fe^{2+}$	
Oxidation of H_2S to elemental sulfur (S^0)	$H_2S \rightarrow S^0 + 2H^+ + 2e^-$	
Reduction of Fe^{3+} by H_2S oxidation		$2Fe^{3+} + H_2S \rightarrow 2Fe^{2+} + S^0 + 2H^+$
Precipitation of FeS from Fe^{2+} and H_2S		$Fe^{2+} + H_2S \rightarrow FeS\ (s) + 2H^+$
FeOOH reduction by H_2S with FeS and S^0 formation	$FeOOH + 3H^+ + e^- \rightarrow Fe^{2+} + 2H_2O$ $H_2S \rightarrow S^0 + 2\ H^+ + 2\ e^-$	$2FeOOH + 3H_2S \rightarrow 2FeS + S^0 + 4H_2O$
Oxidation of FeS to sulfuric acid	$S^{2-} + 4H_2O \rightarrow SO_4^{2-} + 8H^+ + 8e^-$ $2O_2 + 8H^+ + 8e^- \rightarrow 4H_2O$	$FeS\ (s) + 2O_2\ (g) + 2H^+\ (aq) \rightarrow Fe^{2+}\ (aq) + H_2SO_4\ (aq)$

Table 1: Redox reactions observed on IRIS devices.

The amount and persistence of FeS in soil can vary depending on hydrologic circumstances and is limited by the availability of Fe and S within the system (Duball et al., 2020). For instance, coastal environments have an abundance of sulfate and FeS formation is restricted by both sulfate reduction and Fe availability (Duball et al., 2020). Berkowitz et al. (2019) determined that the degree of FeS precipitation differed between hydrological conditions, with continuously inundated conditions supporting a higher FeS content than simulated tidal or drought conditions. Under continuously saturated conditions, FeS compounds remain stable, but when exposed to oxygen, iron monosulfides oxidize rapidly through sulfuricization, resulting in the production of sulfuric acid (Berkowitz et al., 2019; Fanning et al., 1989; Wessel & Rabenhorst, 2017). Therefore, the oxidation of FeS has potential to lower soil pH to less than 3.5, which in consequence releases toxic metalloids and hinders vegetation growth (Dent & Pons, 1995; Kölbl et al., 2017; Wessel & Rabenhorst, 2017). Berkowitz et al. (2019) emphasizes that the changes in soil chemistry and morphology due to FeS formation and oxidation need to be considered when

implementing wetland restoration projects. Ideally, restoration designs should prioritize preventing the oxidation of FeS by ensuring the continuation of saturated conditions.

Iron monosulfides can be identified as black or dark grey coatings on soil surfaces and grains distributed throughout the soil matrix (Duball et al., 2020; Wessel & Rabenhorst, 2017). However, due to decomposed organic matter and other dark colored elements such as Mn, additional field tests should be conducted to accurately confirm the presence of FeS in soils (Duball et al., 2020). Duball et al. (2020) suggest that Munsell colors (value ≤ 4 and chroma ≤ 1) could indicate FeS in the soil matrix and should be used with additional field tests such as observing color changes following oxidation or confirming the release of H_2S following acidification.

The smell of H_2S is distinctively similar to rotten eggs and can be confirmed through a "Whiff test" (Darmody et al., 1977; Duball et al., 2020; Wessel & Rabenhorst, 2017). The odor concentration is described on a scale of 0 to 3 and correlates to total S content and the ongoing process of sulfidization (Darmody et al., 1977; Wessel & Rabenhorst, 2017). A rank of 0 suggests a lack of H_2S odor, 1 indicates the odor is only observed if soil is held close to the nose, 2 suggests the odor is present when soil is disturbed or sampled, and 3 signifies the odor is potent enough to smell when walking through the area (Darmody et al., 1977).

FeS concentrations are frequently observed at the interface between soil horizons, particularly in areas with strong redox gradients (Berkowitz et al., 2019; Duball et al., 2020; Jenkinson & Franzmeier, 2006). Their presence can also reflect local carbon availability, especially when located near buried organic matter such as decomposing roots (Duball et al., 2020; Wessel & Rabenhorst, 2017). Identifying FeS in soil horizons is essential for anticipating areas at risk of oxidation if soil is disturbed or drained. A clear understanding of the spatial distribution of FeS,

combined with efforts to maintain saturated conditions in these zones, is crucial for avoiding environmental degradation through sulfuricization and decline in soil quality (Dent & Pons, 1995; Kölbl et al., 2017; Wessel & Rabenhorst, 2017).

1.1.3 Acid Sulfate Soils and Environmental Impacts

Dent & Pons (1995) describes acid sulfate (AS) soils as "the nastiest soils in the world" with an "evil reputation" dating back to the 18th century due to their association with stunted vegetation, strange colors, bad odors, and overall problematic nature when exposed to oxygen. Particularly, the oxidation of sulfides initiates sulfuricization and can lead to severe environmental degradation if the rate of acid production is greater than the buffering capacity of the soil (Dent & Pons, 1995; Fanning et al., 1989; Wessel & Rabenhorst, 2017). AS soils most commonly form in wetlands that are influenced by a source of salinity, such as brackish waters or marine environments where sulfate is reduced to sulfide under anaerobic conditions (Fanning et al., 1989, 2017; Wessel & Rabenhorst, 2017). However, they may still develop in freshwater environments if sufficient sulfur and reducing conditions are present.

A general definition for AS soils was developed at the 1973 Acid Sulfate Soil Symposium and is as follows: "all soils in which sulfuric acid may be produced, is being produced, or has been produced in amounts that have a lasting effect on main soil characteristics" and form under severely reducing conditions (Dent & Pons, 1995; Fanning et al., 2017). This definition highlights that AS soils are classified not solely by their current acidity, but by the potential to generate acidity when oxidized.

Potential AS soils containing hypersulfidic material can remain nonacidic under anaerobic waterlogged conditions and support wetland ecosystems (Kölbl et al., 2017). However, these

soils pose a major environmental threat when exposed to oxygen, such as during drought conditions or drainage for agricultural or urban development (Dent & Pons, 1995; Kölbl et al., 2017; Wessel & Rabenhorst, 2017). Once exposed to oxygen, hypersulfidic material transforms into sulfuric material which triggers the release of sulfuric acid and mobilizes metals and metalloids that can contaminate ground and surface waters (Fanning et al., 2017; Kölbl et al., 2017). Thus, nonacidic soils with a high sulfide content can still produce large amounts of sulfuric acid when oxidized and be classified as AS soils (Kölbl et al., 2017; Pons, 1973). Additionally, reducing conditions can be reinstated after oxidation if the soil is re-saturated and allows for the reduction of sulfate to sulfide (Kölbl et al., 2017).

Process	**Half reactions**	**Full reaction**
Oxidation of FeS to sulfuric acid	$S^{2-} + 4H_2O \rightarrow SO_4^{2-} + 8H^+ + 8e^-$ $2O_2 + 8H^+ + 8e^- \rightarrow 4H_2O$	$FeS\ (s) + 2O_2\ (g) + 2H^+\ (aq) \rightarrow Fe^{2+}\ (aq) + H_2SO_4\ (aq)$
Oxidation of FeS_2 to sulfuric acid	$2S^{-1} + 7H_2O \rightarrow 2SO_4^{2-} + 14H^+ + 14e^-$ $7/2\ O_2 + 14H^+ + 14e^- \rightarrow 7/2\ H_2O$	$FeS_2\ (s) + 7/2\ O_2\ (g) + 7/2\ H_2O\ (l) + 2H^+\ (aq) \rightarrow Fe^{2+}\ (aq) + 2H_2SO_4\ (aq)$

Table 2: Production of sulfuric acid by FeS and FeS_2 oxidation.

Following oxidation, sulfate (SO_4^{2-}) reacts with available protons to form sulfuric acid ($SO_4^{2-} + 2\ H^+ \rightarrow H_2SO_4$) which contributes to severe soil acidification, lower pH, and mobilization of toxic elements (Dent & Pons, 1995; Kölbl et al., 2017; Wessel & Rabenhorst, 2017).

These soils form if the buffering capacity of the soil is outpaced by the acidification process that occurs when oxidized (Dent & Pons, 1995). Buffering capacity refers to the soil's ability to resist changes in pH through basic compounds such as carbonates or silicate minerals such that, if these buffering agents are insufficient or depleted, acidification can rapidly progress following oxidation. If there are favorable conditions for leaching and drainage, the formation of AS soils may be accelerated due to the oxidation of sulfides (Pons, 1973).

1.1.4 Redox Reactions in Soil

The redox potential (Eh) is defined by the voltage difference between a reference and working electrode. This measurement represents the tendency of the system to gain or lose electrons, which directly influences soil chemistry, metal solubility, nutrient availability, and microbial activity (Berkowitz et al., 2019; Husson, 2013). Natural fluctuations in Eh occur due to varying moisture levels, organic matter content, and microbial respiration, which create dynamic redox gradients both spatially and temporally (Berkowitz et al., 2021; Husson, 2013; Rabenhorst & Hively, 2009).

As soils become saturated and oxygen is depleted through microbial respiration, Eh decreases and reduction reactions become the primary pathway for electron transfer, such as the reduction of Fe^{3+} to Fe^{2+} (Duball et al., 2020). As Eh continues to decline, electron acceptors are reduced in a predictable thermodynamic sequence known as the redox ladder, which reflects their decreasing energy yield (Duball et al., 2020; Zhang & Furman, 2021). The sequence progresses from oxygen, nitrate, manganese oxides, iron oxides, sulfate, and lastly carbon dioxide, which is reduced under the most strongly anoxic conditions (Duball et al., 2022; Fiedler et al., 2007; Hall et al., 2016). Therefore, electron acceptors with higher redox potential, such as oxygen and nitrate, are reduced under weakly reducing conditions, while those with lower Eh, such as iron and sulfate, are less energetically favorable and reduced only under more extreme conditions (Duball et al., 2020; Sapkota et al., 2022; Zhang & Furman, 2021).

Eh measurements can be used to estimate redox processes, differentiate soils, and predict the behavior of soils over time (Fiedler et al., 2007). However, Eh measurements must be interpreted with caution due to spatial variability and electrode instability (Rabenhorst & Hively, 2009). Multiple electrodes and repeated measurements are recommended to better capture the

heterogeneity of natural systems (Rabenhorst & Hively, 2009).Despite these challenges, Eh remains a useful tool for monitoring redox driven geochemical transformations in soils.

Understanding where Fe and S fall on the redox ladder offers important context for interpreting mineral transformations in reducing soils. Iron is reduced at a higher Eh than sulfate, meaning that iron oxides will reduce first, releasing Fe^{2+} into solution. As conditions become more reducing, sulfate is reduced to sulfide (S^{2-}) and can reacts with Fe^{2+} to form iron sulfide minerals such as FeS and FeS_2 (Duball et al., 2020; Rabenhorst et al., 2010). These sequential transformations not only influence mineral assemblages but also affect trace metal mobility, pH, and nutrient cycling (Berkowitz et al., 2019; Duball et al., 2020; Hall et al., 2016). Essentially, redox potential improves our ability to predict how soils will respond to environmental changes such as long-term saturation, drainage, or restoration (Husson, 2013).

1.2 Geophysics

1.2.1 Foundations and Comparisons of Geophysical Methods

Geophysical methods are widely used for subsurface mapping and investigations across several fields such as environmental studies, hydrogeology, and engineering. Common geophysical methods include electrical resistivity tomography (ERT), ground penetrating radar (GPR), and electromagnetic induction (EMI) and each have their own unique strengths and limitations but are highly effective and beneficial for subsurface studies.

GPR uses high-frequency electromagnetic waves to detect contrasts in dielectric permittivity, allowing for the identification of subsurface features such as voids or stratigraphic layers (Van De Vijver et al., 2015). However, its effectiveness is strongly influenced by the electrical conductivity of the soil. High-conductivity soils, such as those with significant clay content or

high salinity, can severely attenuate the radar signal, limiting the depth of investigation and the resolution of subsurface imaging (Doolittle & Collins, 1998; Pathirana et al., 2023). Additionally, GPR is less effective in areas with thick vegetation or rough terrain, where signal interference and logistical constraints can hinder data collection, such as the size and maneuverability of the GPR apparatus.

ERT provides high-resolution data and is particularly effective for delineating variations in lithology or groundwater (Coscia et al., 2011; McLachlan, Blanchy, Chambers, et al., 2021; Miller et al., 2008). The process works by injecting electrical currents into the ground through electrodes and measuring the voltage difference to map resistivity (McLachlan, Blanchy, Chambers, et al., 2021). This is an effective method, but can be labor-intensive, requiring the deployment of multiple electrodes, careful calibration, and significant time for data acquisition and processing. Mapping large areas with ERT often necessitates multiple surveys and overlapping datasets to ensure accuracy, further adding to the time and logistical demands (Miller et al., 2008).

In hydrogeophysical studies, ERT is a more commonly used technique than low-frequency domain EMI, however, EMI is becoming increasingly popular (Doolittle & Brevik, 2014; McLachlan, Blanchy, & Binley, 2021). By requiring less effort for setup and operation, EMI significantly reduces the time and resources needed to complete surveys, enabling broader coverage in a shorter period of time. EMI is a versatile and efficient method for subsurface mapping which allows for rapid data collection over large areas with minimal equipment, labor, and person power. These advantages make EMI a practical choice for large scale investigations, especially when person power is limited. Its portability and minimal operational demands also make EMI well suited for use in autonomous systems, such as deployment on planetary rovers.

This method is particularly advantageous in environments where soil conductivity is of key interest, as it can map soil conductivity variations faster than ERT and GPR. These advantages made EMI the ideal choice for this project, as it offers a balance between efficiency, practicality, and data reliability.

1.2.2 Introduction to Resistivity

Resistivity and its reciprocal, conductivity, are fundamental geophysical properties that provide valuable insights into subsurface conditions. Since the early 20th century, these properties have been used to characterize features such as lithology, bedrock depth, depth and physicochemical characteristics of aquifers, and other geological complexities (Doolittle & Brevik, 2014; McNeill, 1980a, 1980b; Pathirana et al., 2023; Toushmalani, 2010). Due to their broad applicability, resistivity and conductivity properties are utilized in subsurface investigations across fields such as environmental science, hydrogeology, geotechnical engineering, and archaeology (Doolittle & Brevik, 2014; Pathirana et al., 2023; Toushmalani, 2010).

Resistivity and conductivity are influenced by several physical and chemical factors, including soil texture, moisture content, mineral composition, porosity, salinity, and temperature (Corwin & Lesch, 2005; Doolittle & Brevik, 2014). Conductivity, in particular, depends on an electrolytic process where electric currents travel through moisture-filled pores that serve as conductive channels within an insulating matrix (McNeill, 1980a). Variations in saturation, pore water conductivity, bulk density, and grain mineralogy further affect how conductivity and resistivity are measured (Clément et al., 2020; McLachlan, Blanchy, & Binley, 2021; McNeill, 1980a). These factors make resistivity and conductivity valuable indicators of subsurface variability.

To measure these properties, traditional resistivity surveys inject electrical currents directly into the ground using electrodes and record voltage differences to infer subsurface resistivity. In contrast, electromagnetic techniques provide a noninvasive method to measure conductivity by inducing a magnetic field into the subsurface. Materials such as dry sand and solid rock typically exhibit high resistivity and low conductivity, while groundwater and clay layers are more conductive and less resistive (McNeill, 1980a). By analyzing the subsurface response to electrical currents or electromagnetic fields, researchers can map the distribution of materials, detect anomalies, and interpret subsurface features with greater precision.

1.2.3 EMI Device Functionality

EMI devices operate by generating a primary magnetic field, which induces eddy currents in conductive subsurface materials (Doolittle & Brevik, 2014; McLachlan, Blanchy, & Binley, 2021; McNeill, 1980a, 1980b). These eddy currents oppose the primary field and, in turn, create a secondary magnetic field that is measured by the device's receivers (Doolittle & Brevik, 2014; McLachlan, Blanchy, & Binley, 2021; McNeill, 1980a, 1980b). By analyzing the amplitude and phase differences between the primary and secondary fields, and incorporating the inter-coil spacing, the apparent electrical conductivity (ECa) of the subsurface can be calculated (Doolittle & Brevik, 2014; McLachlan, Blanchy, & Binley, 2021; McNeill, 1980a, 1980b).

At low induction numbers, the strength of the secondary magnetic field depends on inter-coil spacing, operating frequency, and subsurface conductivity, with ECa representing the cumulative contributions of soil conductivity across the measured depth interval (Corwin & Rhoades, 1982). The depth of investigation (DOI) is primarily influenced by the spacing between the transmitter and receiver coils, as well as the orientation of the coils relative to the surface (Corwin & Rhoades, 1984; McNeill, 1980b).

In the horizontal coplanar (HCP) configuration, the transmitter and receiver coils are aligned parallel to the surface, forming a vertical magnetic dipole. This orientation produces a magnetic field that loops vertically and can penetrate deeper into the subsurface (McNeill, 1980b). As a result, the HCP configuration is more sensitive to deeper soil layers and less influenced by variations in the first 0.3 meters (Corwin & Rhoades, 1984; McNeill, 1980b). In contrast, the vertical coplanar (VCP) configuration positions the coils upright, creating a horizontal magnetic dipole (McNeill, 1980b). The magnetic field extends parallel to the surface, which supports a greater sensitivity to shallower depths. This allows the VCP configuration to be more responsive to conductivity changes in the top 0.15 meters, while HCP configuration has reduced sensitivity (Corwin & Rhoades, 1984).

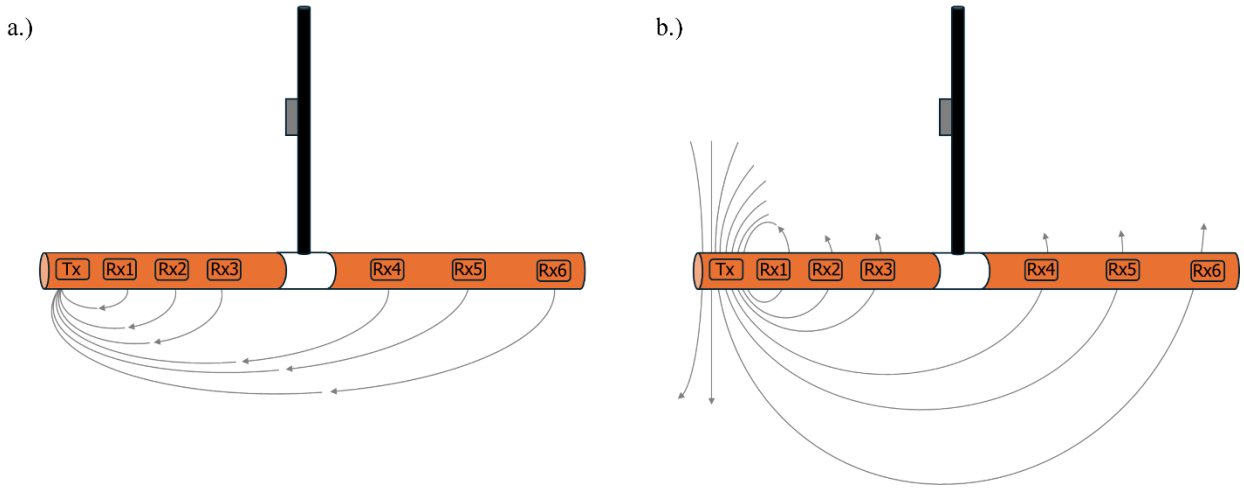

Figure 1: Illustration of the CMD Mini-Explorer 6L electromagnetic induction (EMI) sensor configuration with one transmitter (Tx) and six receivers (Rx).

The difference in sensitivity means that significant conductivity changes within the top 0.3 meters can lead to measurement discrepancies, particularly in complex soil profiles. In inverted profiles, where conductivity is higher near the surface and decreases rapidly with depth, the HCP configuration may underrepresent shallow conductivity variations due to its focus on deeper

layers (Corwin & Rhoades, 1984; McNeill, 1980b, 1980a). Conversely, the VCP configuration may overemphasize the shallow changes due to its sensitivity to near-surface changes. Understanding these limitations is crucial for accurate data interpretation and selecting the appropriate configuration for specific research objectives.

Maxwell's equations, which describe the behavior of electromagnetic fields, can be used to better understand the theoretical foundation of electromagnetic induction measurements. Specifically, Faraday's Law of Induction and Ampère's Law (with Maxwell's Correction) are the two most fundamental principles that predict the behavior of electric and magnetic fields. These laws provide a theoretical framework for time-varying magnetic fields induced currents and how electric currents, in turn, generate magnetic fields. Faraday's Law describes how a changing magnetic field generates an electric field, which, in turn, induces eddy currents in conductive materials during electromagnetic induction. These eddy currents generate a secondary magnetic field, which is the central measurement of EMI conductivity surveys. The mathematical expression of Faraday's Law is displayed by Equation 1.**Equation 1:** Faraday's Law; related time-varying magnetic field to the induced electric field in a conductive medium.

$$\nabla \times E = -\frac{\partial B}{\partial t}$$

Where:

E is the electric field

B is the magnetic flux density

$\frac{\partial B}{\partial t}$ is the rate of change of the magnetic field overtime.

Ampère's Law gives explanation to how magnetic fields arise from both electric currents and changing electric fields. In EMI devices, the induced currents in subsurface material are directly tied to the subsurface conductivity. Ampère's Law with Maxwell's correction states that the curl of the magnetic field is proportional to the current density and the displacement current from a changing electric field. The magnetic fields they generate can be measured and used to map such properties. Ampère's Law (with Maxwell's correction) is expressed in Equation 2.

Equation 2: Ampère's Law with Maxwell's correction, which incorporates the displacement current term to account for time-varying electric fields. This formulation is necessary to describe the propagation of electromagnetic waves in the subsurface.

$$\nabla \times H = J + \frac{\partial D}{\partial t}$$

Where:

H is the strength of the magnetic field

J is the current density (the amount of electric current flowing per unit area in the ground or material)

D is the electric displacement field

$\frac{\partial D}{\partial t}$ is the displacement current (rate of change of the electric field over time)

Regarding EMI devices, McNeill (1980b) shows that the apparent conductivity (σ_a) can be derived using low induction number approximation. The formula (Equation 3) is based on the relationship between the secondary magnetic field (H_s) generated by eddy currents, and the primary magnetic field (H_p) produced by the transmitter coil:

Equation 3: Apparent electrical conductivity (σ_a) derived under the low induction number approximation, as presented by McNeill (1980b). The equation relates the ratio of secondary to primary magnetic fields to conductivity, incorporating system geometry and signal frequency.

$$\sigma_a = \frac{4}{\mu_0 \omega s^2} \cdot \frac{H_s}{H_p}$$

Where:

H_s is the secondary magnetic induced by eddy currents

H_p is the primary magnetic field generated by the transmitter

μ_0 is the magnetic permeability of free space ($4\pi \times 10^{-7}$ H/m)

$\omega = 2\pi f$ is angular frequency of the transmitted electromagnetic signal where f is the frequency

s is the distance between the transmitter and receiver coils

The apparent conductivity measured by EMI is strongly influenced by subsurface redox conditions, as redox reactions govern the concentration of mobile ions and formation or dissolution of conductive metals. Under reducing conditions, iron oxides are reduced to soluble Fe^{2+}, and sulfate may be reduced to sulfide, both of which increase the ionic porewater concentration and lead to an increase in conductivity (Atekwana & Slater, 2009). These changes in the electrical properties of soil, driven by redox reactions, can be detected by EMI surveys and used to infer the spatial distribution of reducing zones.

When paired with IRIS devices, which provide direct visual evidence of reduction, EMI is capable of assessing redox conditions locally and widespread. This complementary approach is particularly effective in saturated soils and sulfidic systems, as redox gradients control mineral

transformation, nutrient availability, and microbial activity. By mapping the electrical conductivity across the subsurface, EMI offers a practical and non-destructive method of monitoring redox processes and their environmental implications.

Chapter 2: Location and Methods

2.0 Location

2.0.1 Zodletone Spring

Figure 2: Image of Zodletone Spring head in SW Oklahoma.

Zodletone Mountain is located in Kiowa County in southwestern Oklahoma, just southwest of Carnegie, and within the Cambrian-Ordovician Slick Hills Range of the Anadarko Basin near the Wichita Mountains frontal fault zone (Sanders, 1998). The north face of Zodletone Mountain hosts a sulfide and methane-rich artesian spring, known as Zodletone Spring, and flows into the nearby Saddle Mountain Creek, also known as "Stinking Creek" (Apalara et al., 2025; Bachman et al., 2018; Senko et al., 2004). Previous research has suggested that Zodletone Spring is sourced from deep, hydrocarbon-rich brines that have migrated upward through faults and mix with groundwater before discharging at the surface (Sanders, 1998; Younger, 1984).

Sanders (1998) performed geochemical mass balance modeling using NETPATH to support the theory that the spring may be derived from a deep sourced oil brine. The model considered the composition of groundwater near Zodletone Mountain and the composition of a Kiowa County oil field of similar depth in order to reach the final composition of water sampled directly from the spring head (Sanders, 1998). The NETPATH results concluded that mixing 2% of the Kiowa County oil brine and 97% of near-surface water would produce the compositional characteristics of the Zodletone Spring sample (Sanders, 1998). This supports the hypothesis that the spring is ultimately sourced from a deep Anadarko Basin brine that has been diluted by meteoric water.

The spring water is a highly saline, euxinic brine characterized by elevated major ion concentrations and a pH of 7.1 (Apalara et al., 2025; Sanders, 1998). It is enriched with dissolved inorganic carbon due to interactions with subsurface carbonate formations, and degasses CO_2 upon reaching the surface (Younger, 1984). Methane actively bubbles out of the spring, likely derived from deeply buried hydrocarbons, and no detectable oxygen has been found (Apalara et al., 2025; Bachman et al., 2018; Senko et al., 2004). The spring head discharges into a shallow pool, flows through a ~20m path, and enters Saddle Mountain Creek.

Along this path, sediment coloration has been altered from tan to a dark grey due to shifts in redox conditions as seen in Figure 2.

The mineralogy at Zodletone reflects redox-driven sulfur and carbon cycling under anoxic, high-sulfide conditions. These geochemical redox gradients are central to the iron-sulfur world hypothesis, which proposes that such environments supported the emergence of early metabolic processes and mineral-catalyzed organic synthesis (Camprubi et al., 2017; Russel et al., 1994; Schröder et al., 2016; Wächtershäuser, 1992). Thus, the ongoing redox transformations at Zodletone provide a rare opportunity to study modern analogs of biogeochemical cycling under early Earth conditions.

These biogeochemical dynamics are preserved in the mineral distribution and assemblages found at the site, which serve as a record of both abiotic and biologically mediated processes. The mineral assemblages at Zodletone Spring include barite, pyrite, gypsum, calcite, dolomite, quartz, plagioclase, K-feldspar, and jarosite, reflecting dynamic redox conditions (Apalara et al., 2025). The study by Apalara et al. (2025) found that sulfide and sulfate minerals (e.g., pyrite, barite, gypsum) are present only in sediments impacted by the spring, indicating that their formation is directly linked to interactions with the spring water. These minerals being absent from unimpacted sediments emphasize the role the brine is playing in shaping the mineralogical assemblages around and in the spring. Notably, barite precipitation at the surface is considered exceptionally rare, and is one of many complex biogeochemical processes occurring at Zodletone Spring (Donovan & Ditzler, 1986; Sanders, 1998). Surface barite precipitation is thought to be a combination of abiotic and microbial mediated sulfide oxidation (Apalara et al., 2025; Senko et al., 2004). Meanwhile, carbonate minerals such as calcite and dolomite were present in both impacted and unimpacted sediments, suggesting that there is a mix of carbonate

input from nearby carbonate formations and authigenic precipitation driven by the degassing of CO_2 or microbial reduction (Apalara et al., 2025).

These redox-driven mineral transformations at Zodletone offer a modern analog for ancient sulfidic systems and produce measurable geochemical signatures that can be used to assess reducing conditions in the field. The precipitation of iron sulfides and the dissolution of iron oxides supports the expectation that IRIS devices will show indications of reducing conditions through FeS accumulation or iron oxide removal on the films. Likewise, the high ionic concentration of the brine contributes to elevated soil electrical conductivity, which can be detected using electromagnetic induction (EMI) methods. Integrating IRIS device results with EMI conductivity mapping provides an effective approach for monitoring spatial variability in redox conditions across sulfidic environments.

2.1 Methods

2.1.1 Research Objectives

This study combines the geophysical method electromagnetic induction (EMI) with Indicators of Reduction In Soil (IRIS) devices to investigate the relationship between soil electrical conductivity and redox conditions in a highly sulfidic environment. The research focuses on Zodletone Spring in southwestern Oklahoma, an artesian spring emerging from the Anadarko Basin, an extensive oil and gas basin. Zodletone Spring is characterized by elevated concentrations of sulfides in both the water and soil, providing a natural laboratory for studying how geochemical processes influence geophysical signals in the subsurface.

Redox transformations occurring in the soil at this site are primarily driven by the naturally high availability of sulfide and hydrogen, rather than microbial reduction. These reduced compounds

can alter the oxidation states of other elements such as iron, leading to the dissolution of iron oxides and precipitation of iron sulfide minerals. To evaluate these redox dynamics, IRIS devices coated in iron oxide paint were deployed to obtain both visual and quantitative evidence of reduction. Paint removal and the formation of iron monosulfides on the films serve as indicators of reducing conditions in the soil, providing insights into active redox activity.

Additionally, EMI surveys were conducted to measure apparent electrical conductivity across the study area. This non-invasive geophysical method provides the opportunity to map spatial variations in conductivity, which can be influenced by factors such as ion concentrations, moisture, and the presence of conductive minerals formed through redox reactions. Integrating EMI data with IRIS results allows for a novel approach to delineating subsurface redox zones and identifying the spatial extent of reduced environments.

The ultimate objective of this research is to evaluate the potential of EMI as a tool for identifying redox-active zones in extreme environments, on Earth and potentially on other planets such as Mars. Environments with strong redox gradients, high sulfide concentrations, and active geochemical cycling, such as Zodletone, serve as valuable analogs for early Mars and other planetary bodies where life-supporting conditions may have existed. Redox interfaces are particularly important targets in astrobiology, as they can concentrate energy sources, catalyze organic reactions, and preserve biosignatures in minerals such as iron sulfides. If adapted for rover use, EMI could help identify subsurface redox gradients associated with past water activity, offering insight to geochemical evolution and potential extraterrestrial habitability.

In this study, it is hypothesized that EMI data will reveal higher conductivity values in areas and depths where redox reactions are actively occurring due to the accumulation of dissolved ions and increased ion mobility. In contrast, lower conductivity values are expected in zones where

redox activity is limited or absent, reflecting more stable conditions. The degree of redox activity will be assessed using IRIS devices which provide both visual and quantitative indictors of reduction.

2.1.2 Data Collection

EMI data collection using the CMD Mini-Explorer 6L from GF Instruments and was selected for its efficiency, portability, and single-operator usability. This non-invasive device simultaneously measures apparent electrical conductivity (ECa) at six discrete depth intervals, making it particularly useful for assessing redox activity across a soil profile. However, because ECa values represent a bulk average response, inversion modeling is necessary to accurately determine vertical variations in conductivity and better interrupt redox interfaces at depth. Raw ECa measurements can be converted to true electrical conductivity (EC) through this process, allowing for a more accurate representation of subsurface conditions.

Due to the dynamic nature of the spring, a repeatable grid-based survey design was not feasible. Surface water pools shift seasonally, and cattle consistently remove survey markers installed at the site. As a result, a flexible transect-based approach was more appropriate than a fixed grid layout. Surveys were conducted by walking with the EMI and control unit in hand, keeping the sensor as close to the ground as possible to minimize airspace interference (**Figure 3**). The instrument was operated on its shortest dipole configuration, collecting measurements at depth intervals of 0.3, 0.5, 0.8, 1.1, 1.6, and 2.3 meters. High density sampling was achieved by configuring the EMI to perform measurements every 0.2 seconds. Data point locations are shown in **Figure 4** and were clustered to avoid overcrowding and provide a clearer visualization, and each mapped point represents an average location of at least five individual measurements.

Figure 3: Demonstration of EMI in use near Zodletone Spring head.

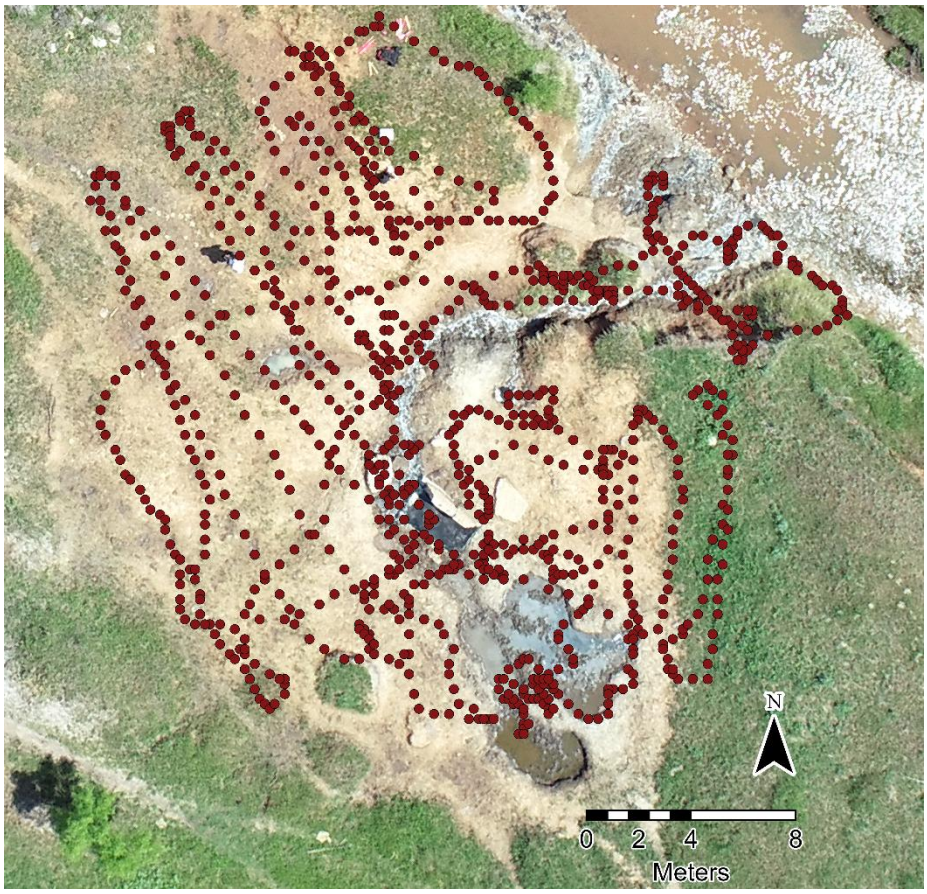

Figure 4: Aerial overview of Zodletone Spring with electromagnetic induction (EMI) survey data points overlain.

To complement the EMI surveys, IRIS devices were installed to visually and quantitatively assess iron and sulfur redox reactions across the study area. The devices, which are PVC film strips coated in iron oxide paint, were purchased from Advanced Iris Oxides (IRISOxides.com) and were constructed with a mix of ferrihydrite and goethite as formulated in Rabenhorst & Burch (2006). Four sites, labeled A, B, C, and D, were selected for IRIS device installation based on zones of varying conductivity. Sites A and C represent areas of high conductivity, site D represents moderate conductivity, and site B represents low conductivity. Considering the portion

of the IRIS device that is in contact with the soil extends ~0.5m into the subsurface, the inverted EC values at 0.5m depth were used to guide site placements.

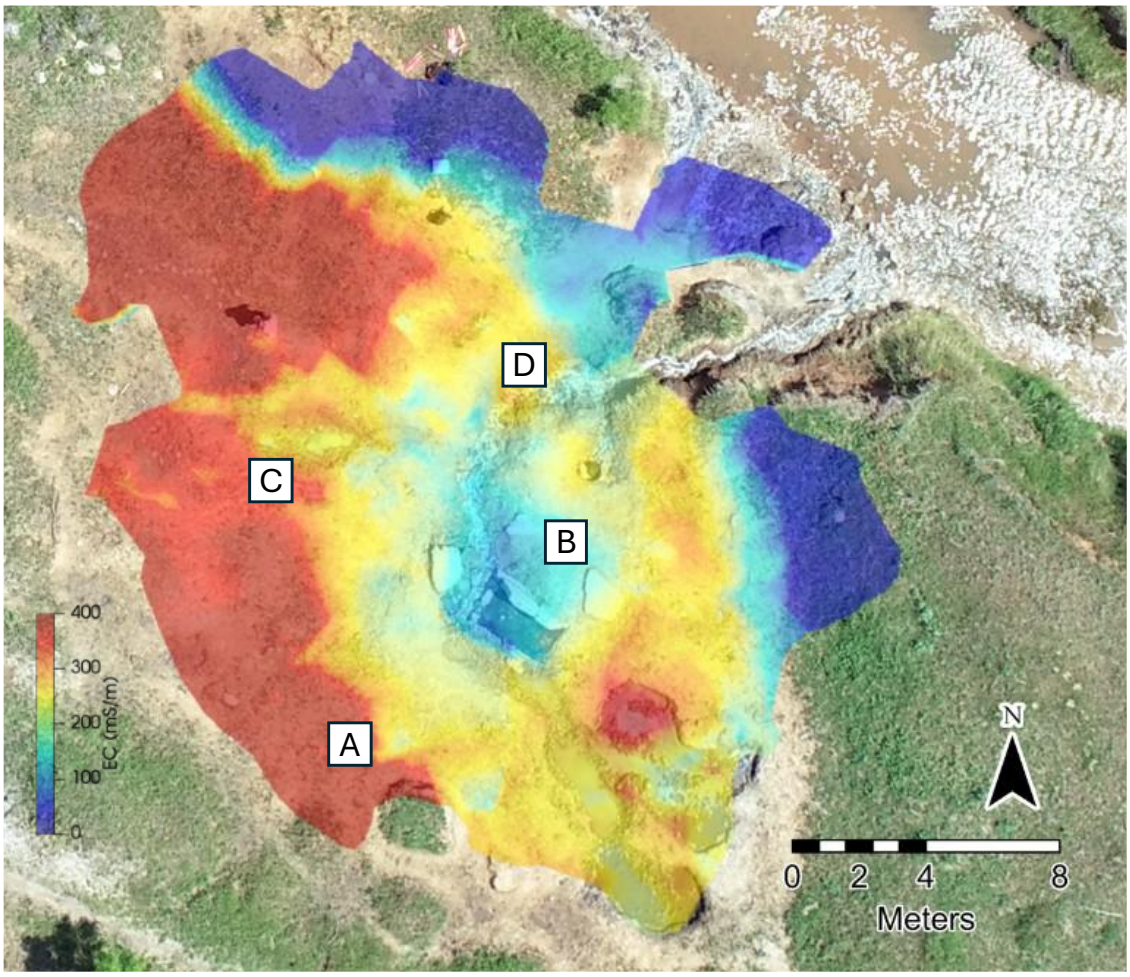

Figure 5: Electromagnetic induction (EMI) conductivity map slice at 0.5m depth after inversion, at 50% transparency overlain on an aerial view of Zodletone Spring.

The IRIS devices were prepped by rolling up the film strips and placing them into a delivery tube. A pilot hole was created using a 1-inch diameter tube, and then the loaded delivery tube was placed into the hole. A hook was used to keep the film in place, while the delivery tube was removed, allowing the film to uncurl and make direct contact with the surrounding soil.

Figure 6: IRIS deployment process.

IRIS devices were installed in clusters at each site with varying deployment times to capture different stages of redox reactions over time. Devices were left in place for durations of 1 hour, 3 hours, and 6 hours to monitor the progressive removal of the iron oxide paint, and precipitation of FeS which are indicators of redox processes occurring in the subsurface. Immediately upon removal, the film strips were gently rinsed with water to remove remaining soil and were scanned using a ScanSnap iX1300 portable scanner to ensure accurate documentation of redox reactions before oxidation could occur. A summary of these reactions is provided in **Table 1** and **Table 2**. The combined use of EMI surveys and IRIS films provides both spatial and temporal resolution of subsurface redox conditions, enabling a stronger link between soil conductivity and active redox processes.

2.2 Data Processing

2.2.1 EMI

The data collected through EMI and IRIS device deployments were processed using a combination of open-source software and machine learning techniques. EMI data was processed using open-source software EMagPy (v1.4.0) and ParaView (v5.13.0-RC1).

In order to create a 3D model, the data must go through an inversion process. Inverting raw ECa data allows for a better understanding of actual EC values and vertical variations, which is necessary when analyzing a particularly heterogeneous subsurface such as our study area. Without inversion, raw ECa values represent a weighted average across depth, which can obscure true depth specific variations and lead to inaccurate interpretations.

EMagPy GUI offers the ability to easily input model parameters and perform inversions to create 3D models (McLachlan, Blanchy, & Binley, 2021). For this study, the input model was performed with settings of 11 layers with 0.2m thickness, and starting EC of 200 mS/m. These settings produced a model that is consistent with patterns seen in the original 2D contour maps and allowed for the analysis of 12 distinct depths (0, 0.2, 0.4, 0.6, 0.8, 1, 1.2, 1.4, 1.6, 1.8, 2, and 2.3m) instead of the 6 depths obtained from the raw data.

The 3D model was then exported as a VTK file and further processed using open-source software ParaView. The cell data was converted to point data to generate a smoother, more continuous model to improve visualization and allow for a more streamlined interpretation. In addition, ParaView was used to create 2D slice views of the 3D model, both horizontally and vertically, to enable cross-sectional analysis of EC distribution at the specific IRIS installation sites.

Inverted EC values at the IRIS locations were manually extracted by the “Select Points by Polygon” feature and exported as a table for further statistical analysis. Due to an extremely large number of datapoints collected from high-density sampling, averaging EC values by depth intervals provided a more manageable and interpretable dataset. This simplification also allowed for clearer comparison of EC variations with depth across all four IRIS sites.

2.2.2 IRIS

The IRIS devices were scanned and analyzed to quantify the redox reactions such as iron oxide removal and iron monosulfides (FeS) precipitation. Analysis was performed using the Trainable Weka Segmentation plug-in from Fiji Is Just (ImageJ), a machine learning based tool for image classification. To classify the IRIS device images, five categories were defined as follows:

1. FeS – Areas with black or dark grey, indicating the precipitation of iron monosulfides (FeS).
2. FeOOH – No reaction. Remain visibly orange and have very little to no ferrihydrite removal or FeS precipitation.
3. FeS/Removed Mix – Denoted by a lighter grey coloration, these regions have a combination of FeS precipitation and minimal ferrihydrite paint removal.
4. Removed – Fully white regions where no FeOOH remains, and no FeS precipitation has occurred.
5. Omit – Imperfections. Areas that should not be considered such as wrinkles formed during deployment, remaining soil, and punch holes.

For each IRIS image, representative pixels were manually selected to train the segmentation model for each category. The trained model was then applied to classify the entire image,

allowing for the quantification of the area covered by each category. A classification threshold of 0.85 was used to ensure high confidence in the pixel assignments. The resulting data provided quantitative metrics that can help determine the extent and distribution of redox gradients and FeS precipitation across the IRIS devices and study area.

2.3 Statistical Analysis

Statistical analyses were conducted using Python (v3.9) with the Pandas, NumPy, Matplotlib and SciPy libraries. Raw data files were organized in an Excel workbook, with each site's (A, B, C, and D) measurements stored on a different sheet. The independent variable (e.g., "Depth (m)") and the dependent variable (e.g., "EC (mS/m)") were extracted from each sheet.

For each site, descriptive statistics including count, mean, standard deviation, minimum, maximum, and percentiles (25^{th}, 50^{th}, and 75^{th}) were calculated. The standard error of the mean (SEM) was also calculated using the formula $SEM = SD/\sqrt{n}$. To assess the relationship between the independent and dependent variables, linear regression analyses were performed using the SciPy library's linregress function to find the slope, intercept, correlation coefficient (R), p-value, and standard error of the regression.

Graphical representations were produced for each site, where scatter plots of the raw data were overlaid with regression lines and error bars representing the grouped means ± SEM. Combined figures were also generated for each IRIS category: data from the individual sites (A, B, C, and D) were plotted as scatter points in different colors, while an additional dataset—representing the combined data from all sites—was depicted with its regression line only. This approach facilitated a direct visual comparison between site-specific variability and the overall trend

across all sites. All summary statistics and plots were automatically saved as CSV and PNG files, respectively, ensuring reproducibility and facilitating further examination of the results.

Chapter 3: Results and Discussion

3.0 EMI

3.0.1 Inversion

The processed EMI dataset and IRIS observations were used to evaluate how EC varies with depth across the study area and whether those patterns correspond to redox activity. The following section presents the trends in EC across the four selected IRIS sites.

Prior to interpretation, it is important to evaluate the accuracy of EMI inversion results. Inversion error was assessed using the root mean square precent error (RMSPE) provided by EMagPy's GUI, which quantifies the difference between measured ECa and modeled EC (Figure 7). The RMSE accounting for all coils was 6.004% and the RMSPE values for the individual coils remained below 10%, indicating an acceptable model fit.

The highest errors were observed in the HCP0.3 and HCP0.5 coil readings, likely due to the increased sensitivity of the HCP configuration to deeper subsurface features. Specifically, the HCP0.5 coil exhibited the greatest error (9.58%), which may also reflect the sharp EC contrasts associated with the redox transition zone at ~0.5m depth. Despite these errors, the inversion results are considered reliable for further interpretation.

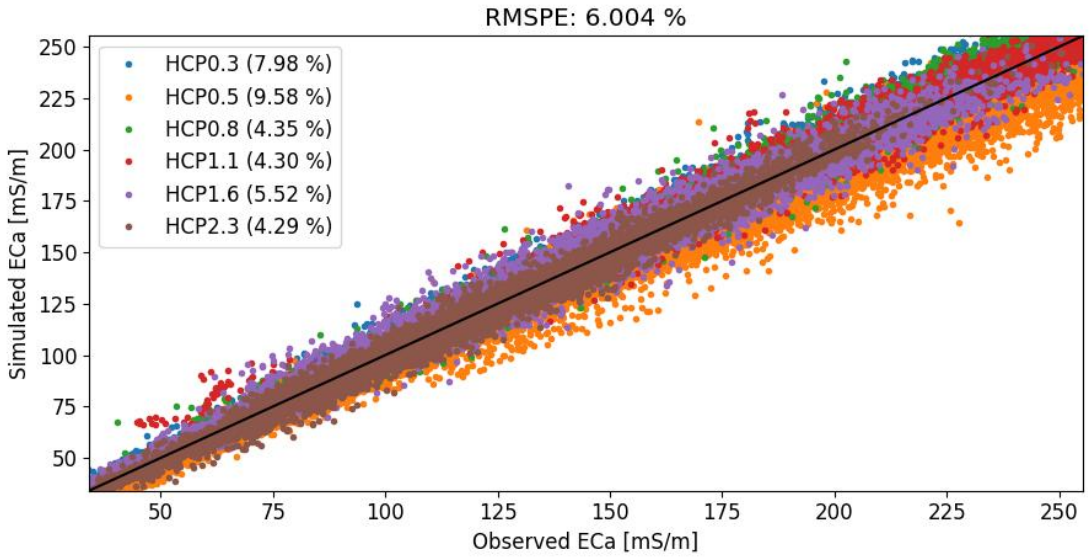

775

776 **Figure 7:** Simulated versus observed apparent electrical conductivity for each of the six EMI
777 coil configurations.

778 With the inversion accuracy deemed acceptable, further analysis focused on visualizing spatial
779 patterns of EC within the subsurface. To capture the horizontal distribution of EC across the
780 entire survey area, 2D slices were extracted from the 3D inversion model at selected depths.
781 Specifically, at 0.2m, 0.4m, 0.6m, and 0.8m were chosen to display key intervals within the
782 uppermost meter of the soil profile, where redox driven conductivity changes were expected to
783 be most pronounced. These slices allow for the assessment of lateral conductivity variation at
784 discrete depths and provide context for interpreting the depth and spatial extent of redox activity
785 near the surface.

786 In addition to horizontal slices, vertical cross sections that correspond to IRIS deployment
787 locations were generated. These cross sections provide a vertical profile of subsurface EC
788 beneath and surrounding each IRIS site, offering insight to the vertical gradients and redox
789 transition zones. Together, the horizontal and vertical profiles provide a complementary

790 perspective on the spatial variability in EC and serve as the basis for interpreting the extent and
791 location of redox activity across the site.

3.0.2 Electrical Conductivity at IRIS Locations

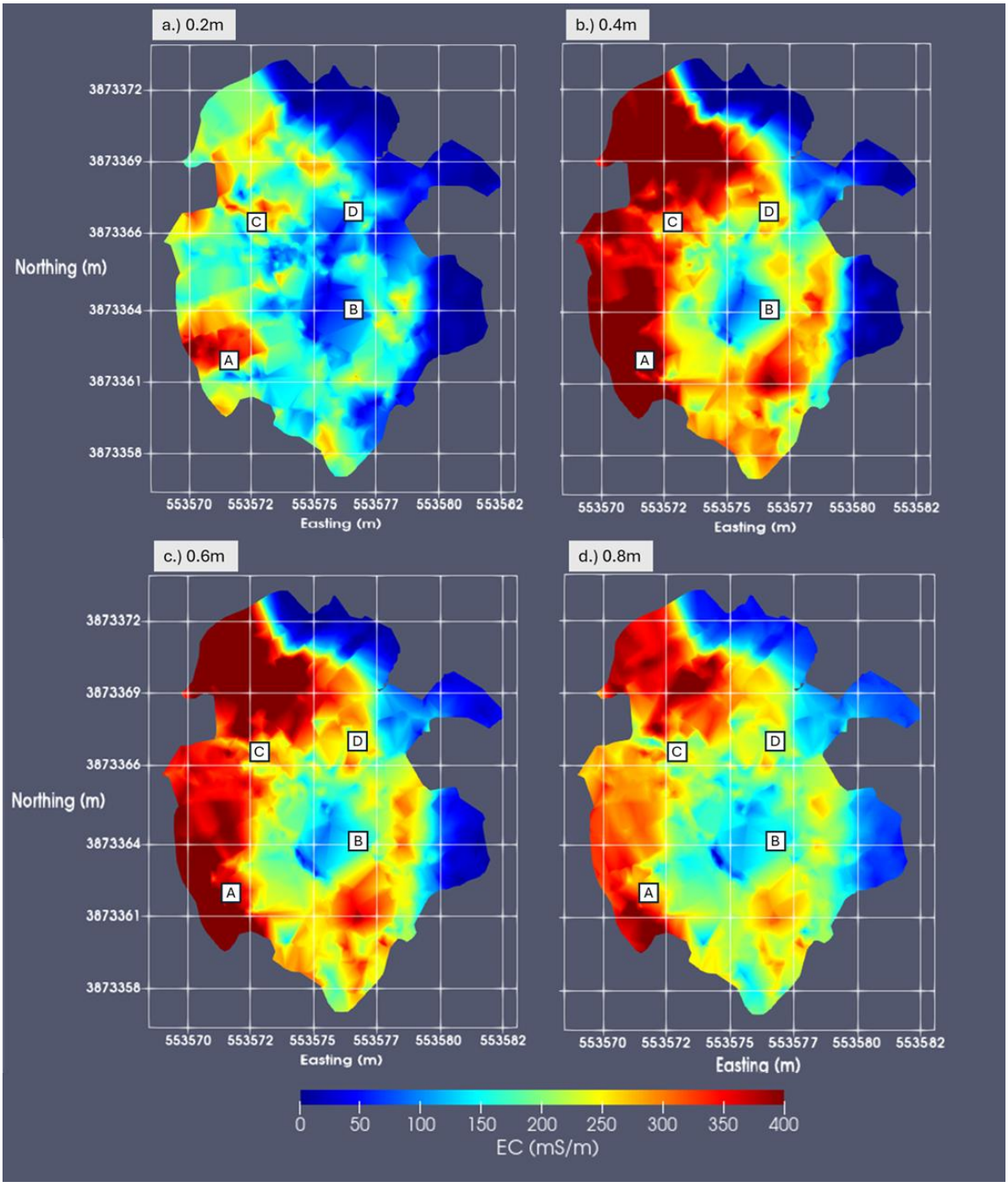

Figure 8: Top view of inverted EMI model with labeled IRIS site locations at depths of a.) 0.2m b.) 0.4m c.) 0.6m and d.) 0.8m.

To further examine the spatial distribution of EC at the IRIS sites with depth, top-down horizontal slices were generated from the inverted EMI model at depths of 0.2m, 0.4m, 0.6m and 0.8m (Figure 8). Each slice includes IRIS site locations and labels (A, B, C, and D), allowing for a direct spatial comparison between conductivity values and IRIS locations. At 0.2m, the regions of low conductivity (0-100 mS/m) near site B and D correspond to flowing surface waters, however the trend can be seen through all depths and is best seen in Figure 5. The most noticeable change in EC is seen between 0.2m and 0.4m with a significant increase across the majority of the study area. However, the most eastern and northeastern sections which are closest to Saddle Mountain Creek remain between ~0-100 mS/m for all depths. There is minimal visual change between 0.4m and 0.6m, although statistical analysis shows that sites A, B, and C had a decline in mean EC while site D exhibited an increase. There is a noticeable decrease in EC across the site between 0.6 and 0.8m, as supported by both visual patterns and statistical results.

These depths were selected based on the results summarized in Table 3, which provides the mean EC at each site for several depths obtained from the inverted model. Sites A and C reach a maximum mean EC at 0.4m (419.2 ± 58.5 and 458.7 ± 11.0 mS/m, respectively), while site D had a maximum of 232.9 ± 27.8 mS/m at 0.6m. Site B exhibited a maximum mean EC of 161.7 ± 7.1 mS/m at a depth of 1.6m, suggesting that the redox transition zone may be deeper in that region. Notably, the lowest mean EC values for sites B, C, and D were found at the surface (0m), while site A's minimum was at 2.3m. Because these values were derived from the shallowest and deepest layers of the inversion model, they may be more susceptible to boundary related errors. Ultimately, the figures and table both provide insight into the lateral and vertical variation of EC and support the depth-specific trends observed in the summary statistics.

	Site A	**Site B**	**Site C**	**Site D**
Depth(m)	**Mean EC ± Std. Dev. (mS/m)**	**Mean EC ± Std. Dev. (mS/m)**	**Mean EC ± Std. Dev. (mS/m)**	**Mean EC ± Std. Dev. (mS/m)**
0.0	195.5 ± 63.9	8.8 ± 7.0	26.1 ± 14.4	29.6 ± 18.7
0.2	316.8 ± 25.3	57.5 ± 18.8	221.4 ± 18.5	98.5 ± 33.8
0.4	419.2 ± 58.5	106.5 ± 27.4	458.7 ± 11.0	219.9 ± 33.0
0.6	345.4 ± 79.7	101.3 ± 23.2	450.9 ± 12.7	232.9 ± 27.8
0.8	261.2 ± 68.9	108.1 ± 21.0	368.3 ± 14.7	209.9 ± 22.8
1.0	213.9 ± 49.6	124.9 ± 16.9	299.9 ± 11.5	191.5 ± 17.9
1.2	192.4 ± 33.5	141.6 ± 12.3	255.8 ± 8.0	182.4 ± 14.1
1.4	183.2 ± 22.3	154.9 ± 8.8	229.2 ± 5.4	178.7 ± 11.5
1.6	175.0 ± 16.9	161.7 ± 7.1	213.0 ± 3.5	173.6 ± 12.3
1.8	139.9 ± 16.8	144.0 ± 5.8	191.0 ± 3.1	145.1 ± 19.0
2.0	50.8 ± 9.3	99.5 ± 11.1	100.7 ± 6.9	63.6 ± 33.9
2.3	40.4 ± 12.8	92.0 ± 12.5	78.5 ± 8.3	55.1 ± 34.2

818 **Table 3:** Mean electrical conductivity (EC) values (± standard deviation, mS/m) from 0-2.3

819 meters, based on inverted EMI data.

Location	**Mean EC (mS/m)** *(unweighted)*	**Std. Dev. (mS/m)**	**Minimum (mS/m)**	**Maximum (mS/m)**	**Range (mS/m)**	**n**
All Sites	180.5	100.2	0.3	512.4	512.1	6005
Site A	223.6	110.9	6.6	512.4	505.8	1254
Site B	118.4	35.2	2.0	168.6	166.6	1790
Site C	261.4	122.0	7.8	478.6	470.9	1172
Site D	162.8	61.6	0.3	277.2	276.9	1747

Table 4: Summary statistics of inverted EC values at each IRIS site (A, B, C, and D).

The mean electrical conductivity varied between locations, with site B having the lowest mean and standard deviation (118.4 ± 35.2 mS/m, n=1790) and values ranging from 2.0-168.6 mS/m (min-max). Site D had the second lowest mean (162.8 ± 61.6 mS/m, n=747), and a range of 0.3-277.2 mS/m, followed by site A (223.6 ± 110.9 mS/m, n=1254) with a range of 6.6-512.4 mS/m. Site C had the highest mean EC and standard deviation (261.4 ± 122 mS/m, n=1172) and a min-max of 7.8-478.6 mS/m. The entire dataset (All Sites) had a range of 512.1 mS/m and a mean of 180.5 ± 100.2.

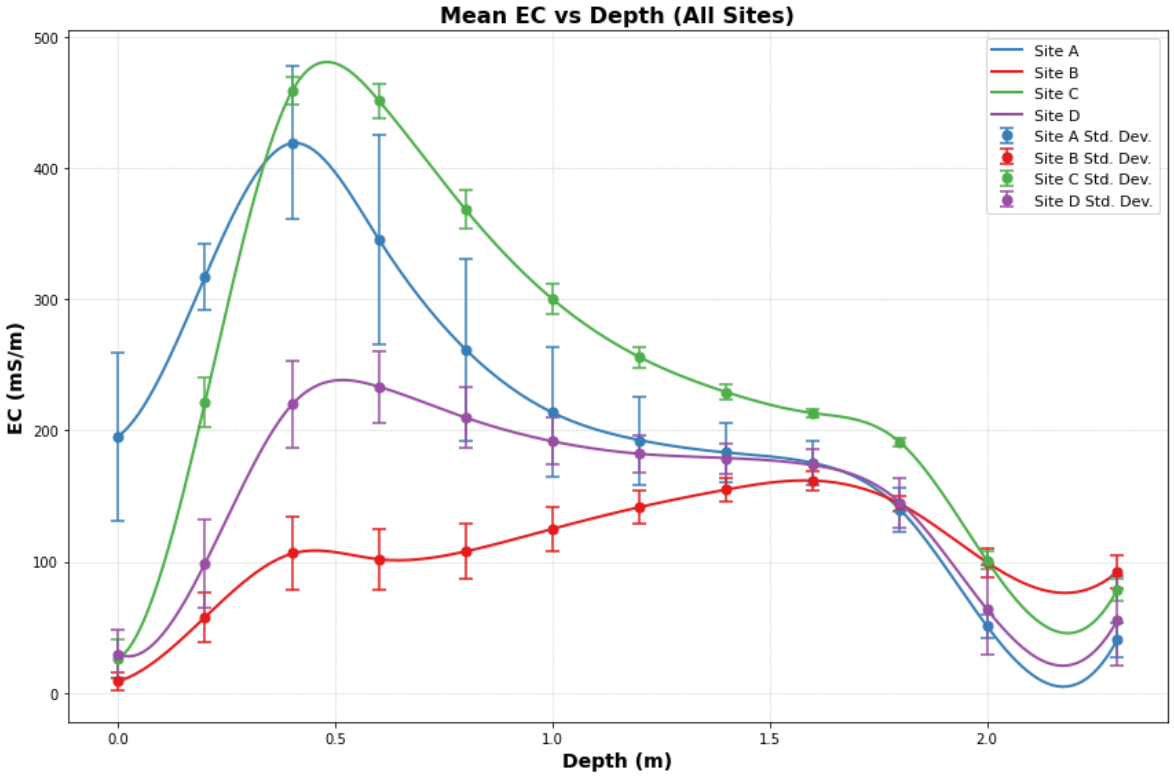

828

829 **Figure 9:** Mean EC versus depth for each IRIS site, based on inverted EMI data.

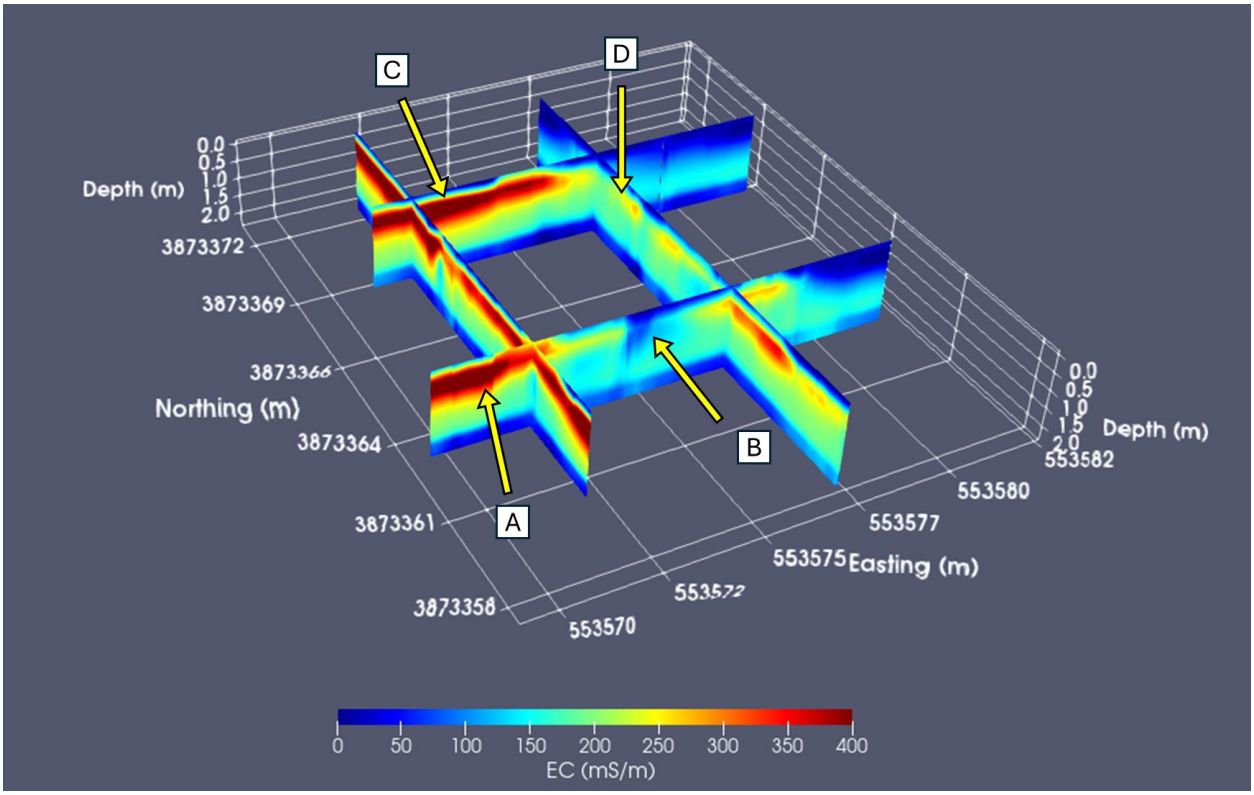

Figure 10: Cross-sectional EMI inversion results through each IRIS site, with labeled site locations indicated by arrows.

Figure 10 shows the cross sectional distrubution of EC across the site and the specific IRIS locations. Although the highest mean EC in the study area was found to be 512.4 mS/m, a range of 0-400 mS/m was established in order to better display small variations in EC. The EMI cross-sections shown here follow the same alignment as ERT transects used in a separate project at this site. Although ERT results are not included in this study, their alignment ensured consistency across investigations for future collaborations.

3.1 IRIS

IRIS films were deployed in four sites, A, B, C, and D, for durations of 1 hour, 3 hours, and 6 hours. By using pixel classification training techniques, we have quantified the redox reactions

that occur on the IRIS films and are able to correlate a relationship between the intensity of reactions and EC variations. All measurements from the IRIS pixel training classification method were performed with a 0.85 confidence threshold. A cumulative area percentage bar graph displaying the mean EC ± standard deviation for each site was created to show the overall differences in reactions in comparison to their EC values (Figure 11).

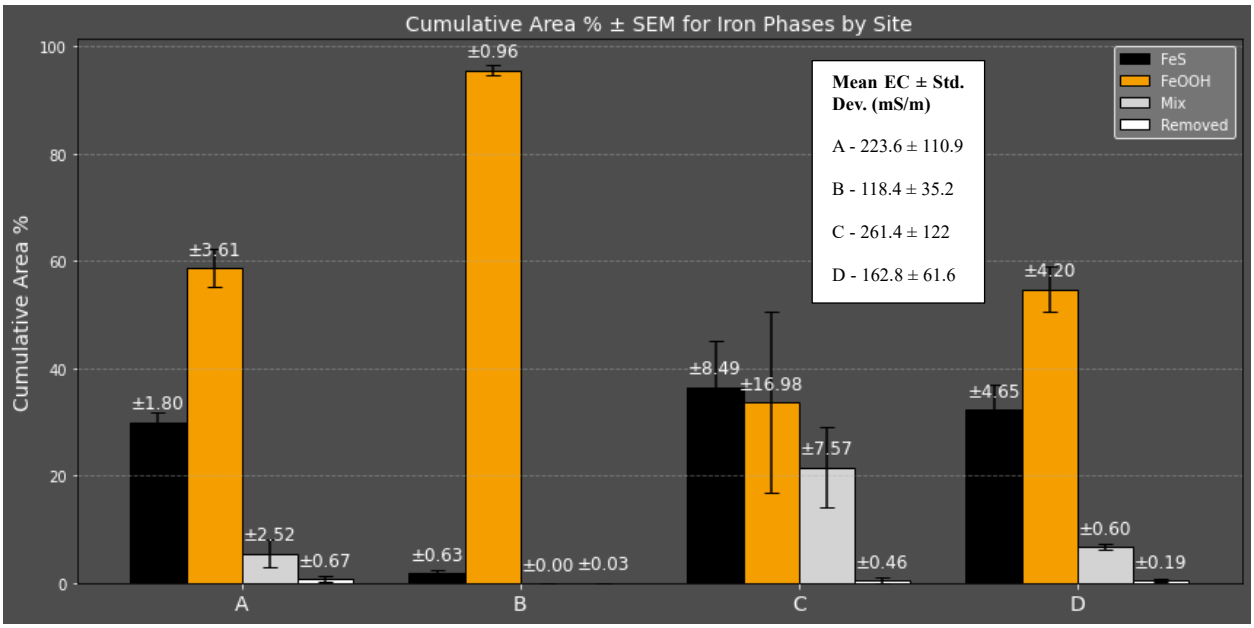

Figure 11: Bar graph showing the cumulative area percentage ± SEM of iron phases (FeS, FeOOH, FeS/Removed Mix, and Removed) for each IRIS site.

3.1.1 Reactions vs Time

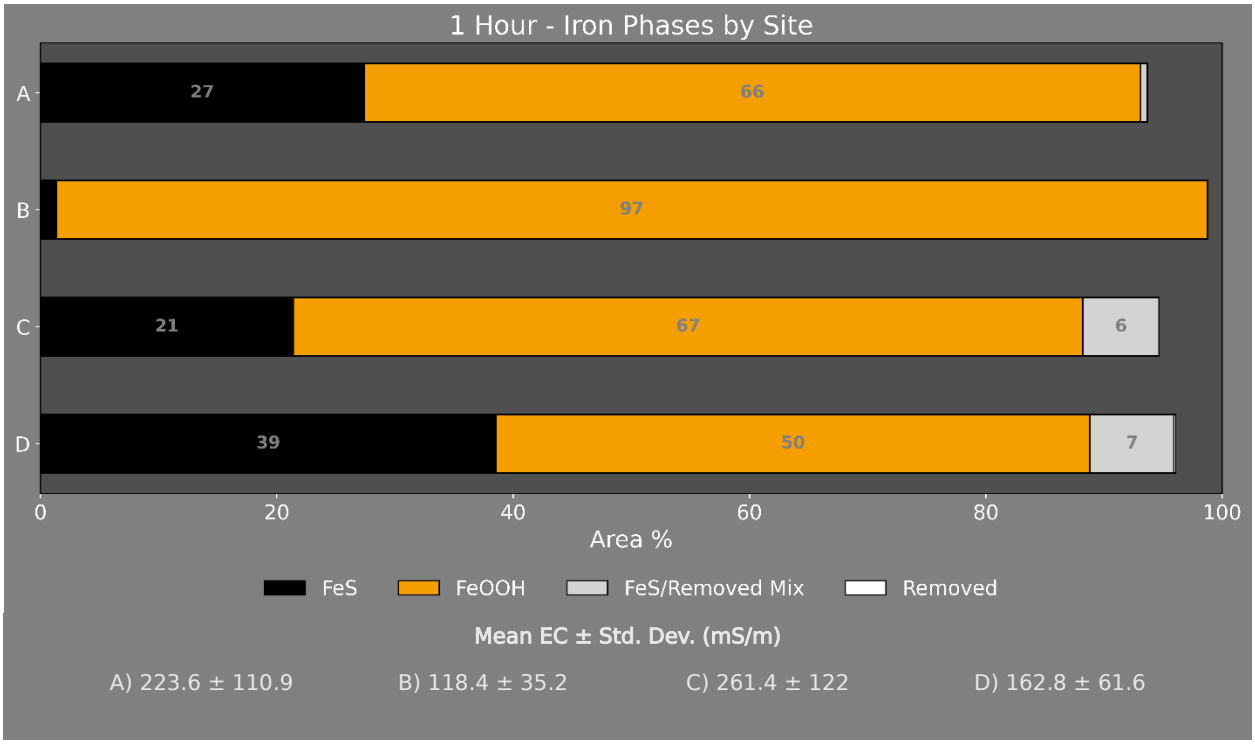

Figure 12: Stacked bar graph showing the area percentage of iron phases (FeS, FeOOH, FeS/Removed Mix, and Removed) observed on IRIS films at each site after 1 hour of deployment.

At 1 hour, FeS precipitation varied across sites, with site D exhibiting the highest FeS concentrations (38.55%), followed by site A (27.39%) and site C (21.4%), while site B had the lowest FeS accumulation (1.36%). The FeS/Removed mix was highest at site D (7.12%), followed by site C (6.43%), and was minimal at site A (0.58%). Site B had no FeS/Removed mix at the 1-hour duration. No fully removed areas were observed at sites A, B, or C after 1-hour, and site D had a very minor fully removed fraction (0.14%). The majority of FeOOH remained intact across all sites, with the highest retention in site B (97.39%), followed by Site C (66.82%), Site A (65.71%), and Site D (50.25%).

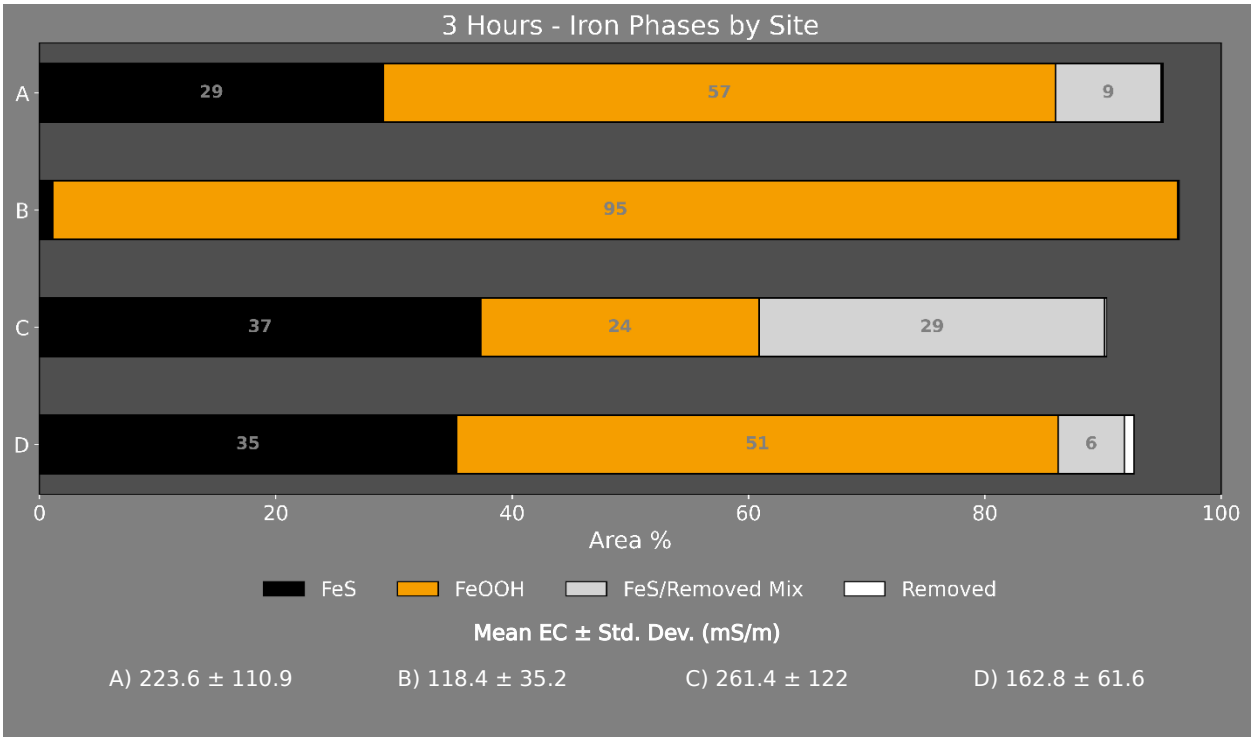

Figure 13: Stacked bar graph displaying the area percentage of iron phases (FeS, FeOOH, FeS/Removed Mix, and Removed) observed on IRIS films at each site after 3 hour.

At 3 hours, FeS precipitation was highest in site C (37.34%), followed by site D (35.32%), site A (29.10%), and was lowest at site B (1.15%). FeS/Removed mix was also the most prominent in site C (29.24%), with site A (8.95%) and site D (5.60%) showing lower amounts, while site B had none. Fully removed FeOOH remained minimal across all sites, with site D showing the highest removal (0.82%), while sites A and C had 0.17% fully removed, and site B had a negligible 0.10%. The proportion of FeOOH remaining varied significantly, with site B retaining the highest amount (95.19%), followed by site A (56.87%), site D (50.88%), and the lowest retention in site C (23.56%).

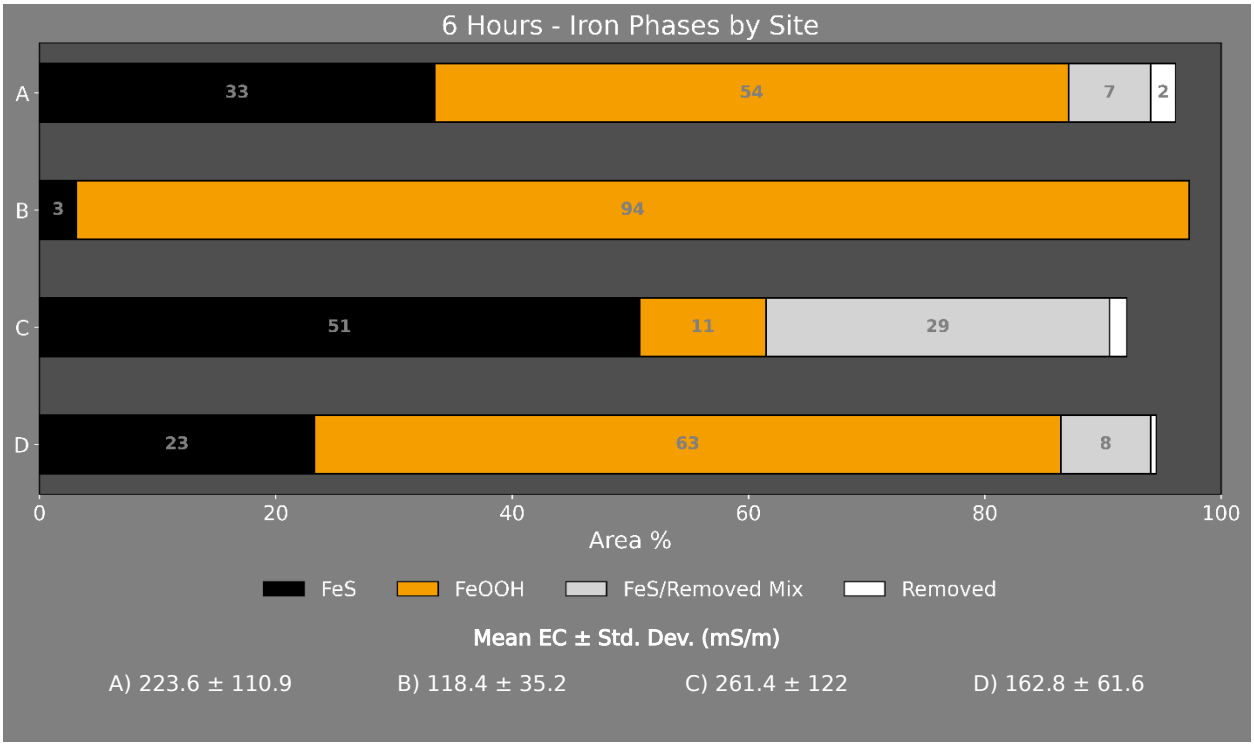

Figure 14: Stacked bar graph illustrating the area percentage of each iron phases on IRIS films at each site following 6 hours of deployment.

At 6 hours, FeS precipitation was highest in site C (50.79%), followed by site A (33.44%), site D (23.28%), and site B with the lowest FeS formation (3.15%). FeS/Removed mix was also most prominent in site C (29.07%), with site D (7.59%) and site A (6.96%), while site B had none. The proportion of FeOOH remaining varied across sites, with the highest retention in site B (94.15%), followed by site D (63.16%), site A (53.64%), and the lowest in site C (10.69%). Fully removed FeOOH areas were minimal, but most notable in site A (2.10%), followed by site C (1.46%), site D (0.48%), and site B (0.01%).

Additional statistical analyses were conducted to determine if there is a significant relationship between changes in iron phases on IRIS films and duration of deployment. In order to best assess time as a limiting factor of FeS precipitation and FeOOH removal, both site specific and

cumulative approaches were used. The site-specific approach gives insight to local variability in phase transformation rates, while the cumulative provides a broader understanding of temporal trends across all locations.

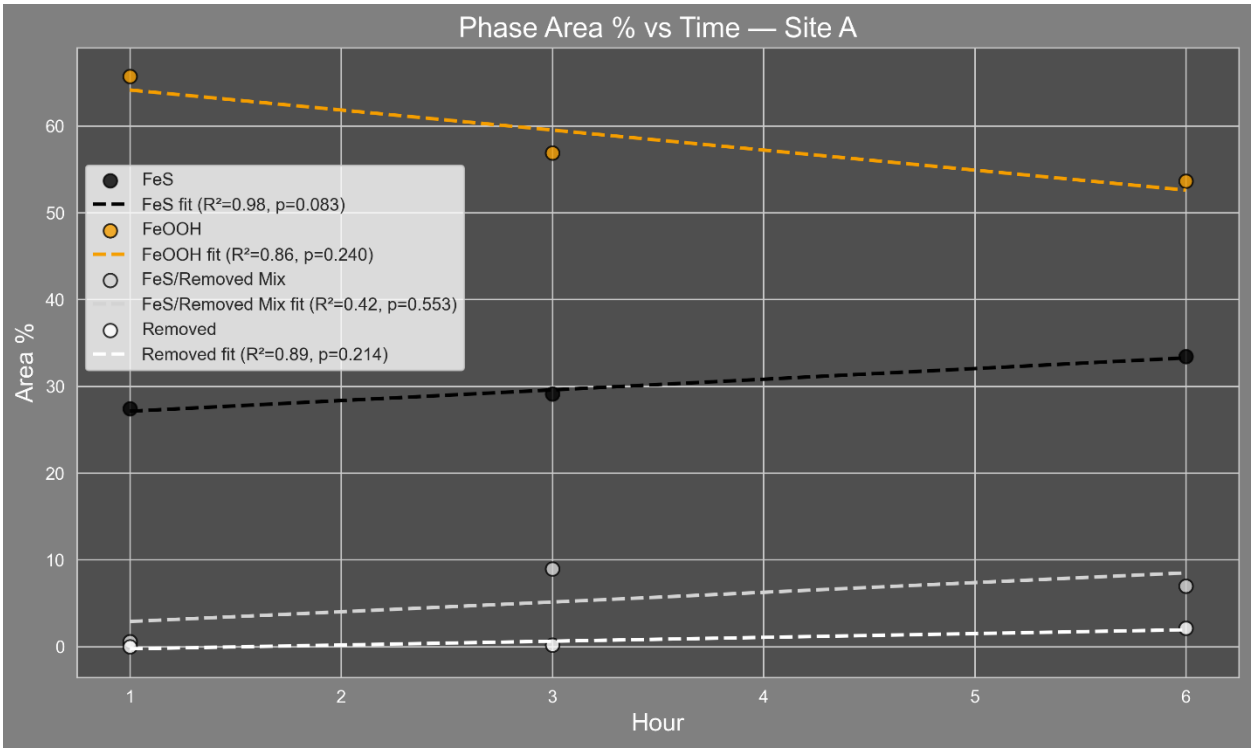

Figure 15: Iron Phase Area % vs Time at Site A. The strongest temporal relationship at site A was observed for the FeS category which showed a high coefficient of determination ($R^2 = 0.98$) and a marginally significant p-value of 0.083. These findings imply that FeS precipitation and accumulation are likely to increase with longer deployment. Conversely, the FeS/Removed Mix phase showed a weak correlation with time ($R^2 = 0.42$, $p = 0.533$) and indicates high variability. FeOOH exhibited a moderately strong, but not statistically significant relationship ($R^2 = 0.86$, $p = 0.240$), as did the Removed category ($R^2 = 0.89$, $p = 0.214$). These results imply that trends are present, however site-specific variability and limited sample size are likely influencing significance levels.

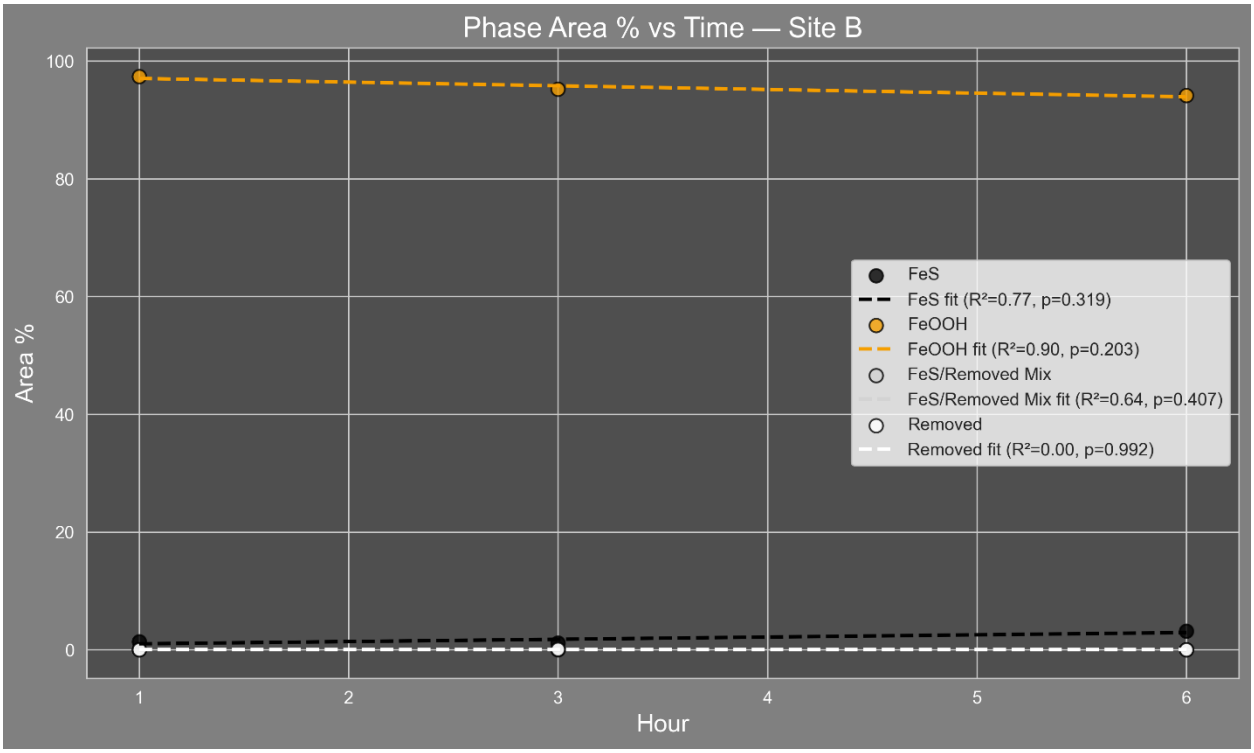

Figure 16: Iron Phase Area % vs Time at Site B.

At site B, regression analysis revealed moderate to strong fits but no statistical significance for the FeOOH ($R^2 = 0.90$, $p = 0.203$), FeS/Removed Mix ($R^2 = 0.64$, $p = 0.407$), and FeS ($R^2 = 0.77$, $p = 0.319$) categories. The Removed category showed no observable trend due to lack of sufficient iron removal from the IRIS films at site B. While the sample size is limited, these findings suggest potential temporal trends for FeS precipitation and FeOOH removal at this location.

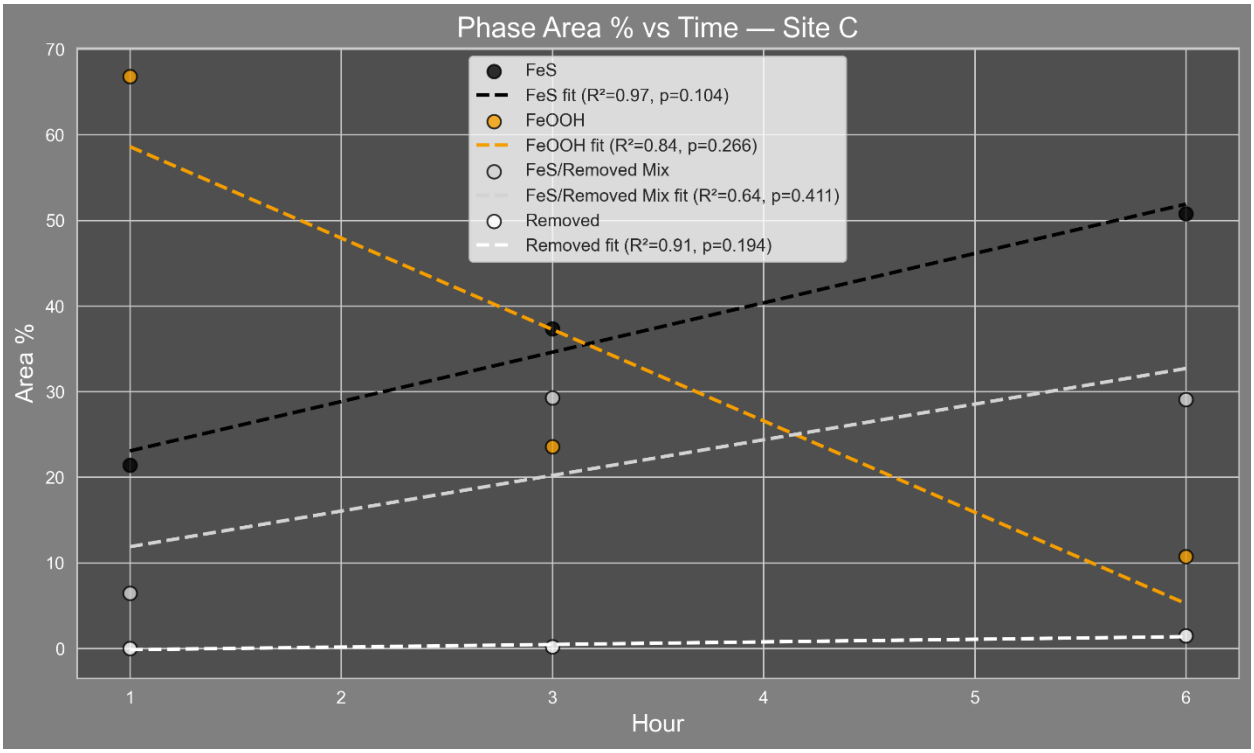

Figure 17: Iron Phase Area % vs Time at Site C.

Regression analysis at site C indicated strong temporal trends, though statistically significance was not achieved. FeS demonstrated the strongest relationship with time ($R^2 = 0.97$, $p = 0.104$), followed by the Removed category ($R^2 = 0.91$, $p = 0.194$) and FeOOH ($R^2 = 0.84$, $p = 0.266$). The FeS/Removed Mix category had the weakest temporal trend ($R^2 = 0.64$, $p = 0.411$). While the R^2 values at site C indicate a strong to moderately strong relationship with time, there is a lack of statistical significance likely due to the limited dataset.

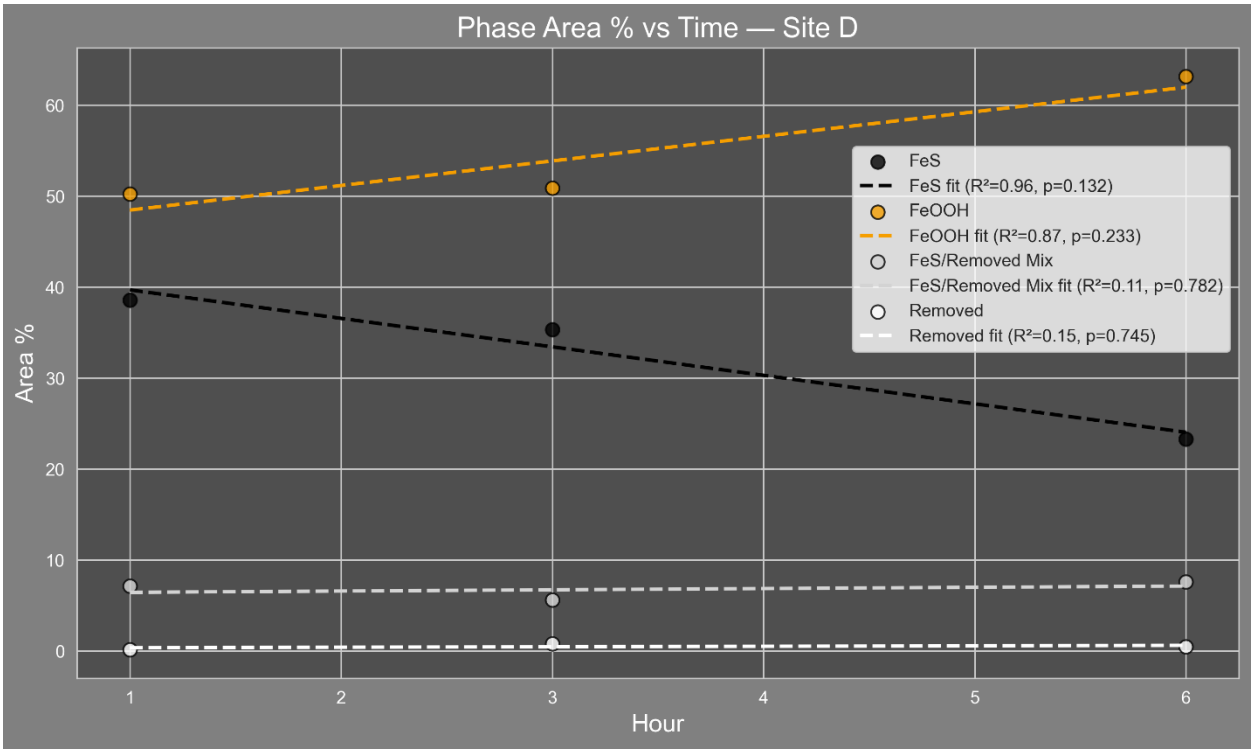

Figure 18: Iron Phase Area % vs Time at Site D.

At site D, FeS exhibited a strong fit ($R^2 = 0.96$) but non-significant p-value ($p = 0.132$) which suggests a potential but inconclusive time-dependent trend. FeOOH showed a similar trend with a moderately strong fit ($R^2 = 0.87$) and p-value of 0.233. In contrast, the FeS/Removed Mix and Removed phases demonstrated very weak correlations ($R^2 = 0.11$, and 0.15, respectively) and high p-values ($p = 0.782$ and 0.745). These results indicate that FeS and FeOOH may undergo changes over time, but additional data is needed to confirm statistical significance.

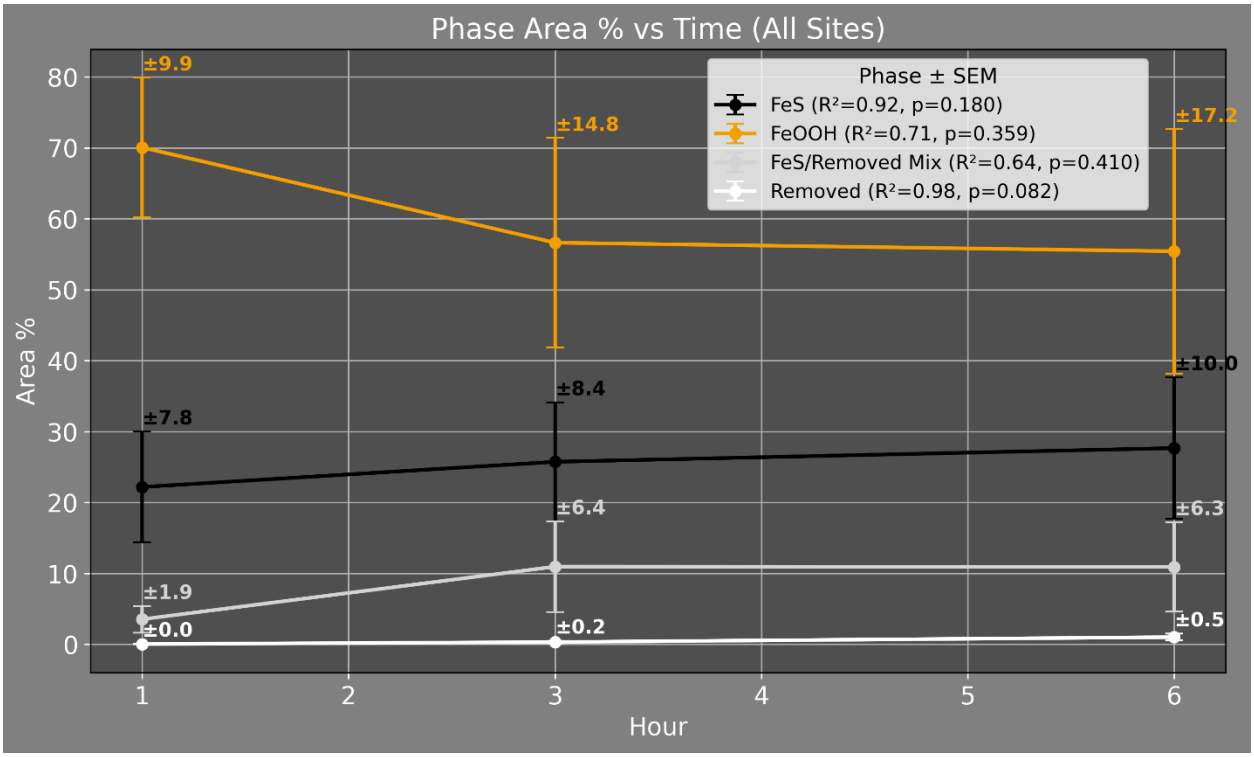

Figure 19: Iron Phase Area % vs Time (All Sites). .

A cumulative analysis was conducted independent of site location and used grouped mean values of each iron phase at 1 hour, 3 hour, and 6 hour to highlight overall temporal trends in iron phase transformations. FeS displayed a strong fit ($R^2 = 0.92$) with a non-significant p-value ($p = 0.180$), and standard error of the mean (SEM) values increasing from ±7.8 at 1 hour, ±8.4 at 3 hours, and ±10 at 6 hours. FeOOH showed a weaker fit ($R^2 = 0.71$, $p = 0.359$) and increasing SEM values with time, indicating greater variation and less temporal consistency. The FeS/Removed Mix phase had a moderate fit ($R^2 = 0.64$, $p = 0.410$) and low SEM values ranging from ±1.9-6.4 while the Removed category had the strongest correlation with time ($R^2 = 0.98$, $p = 0.082$), with SEM variability of ±0.5. However, the low variability for these two categories is likely due to their limited representation in the dataset. These patterns imply that FeS and FeOOH may respond

more predictably to duration of deployment, but high variability limits confidence in time as a sole controlling factor.

3.2 Fe Transformations vs EC

3.2.1 FeS % vs EC

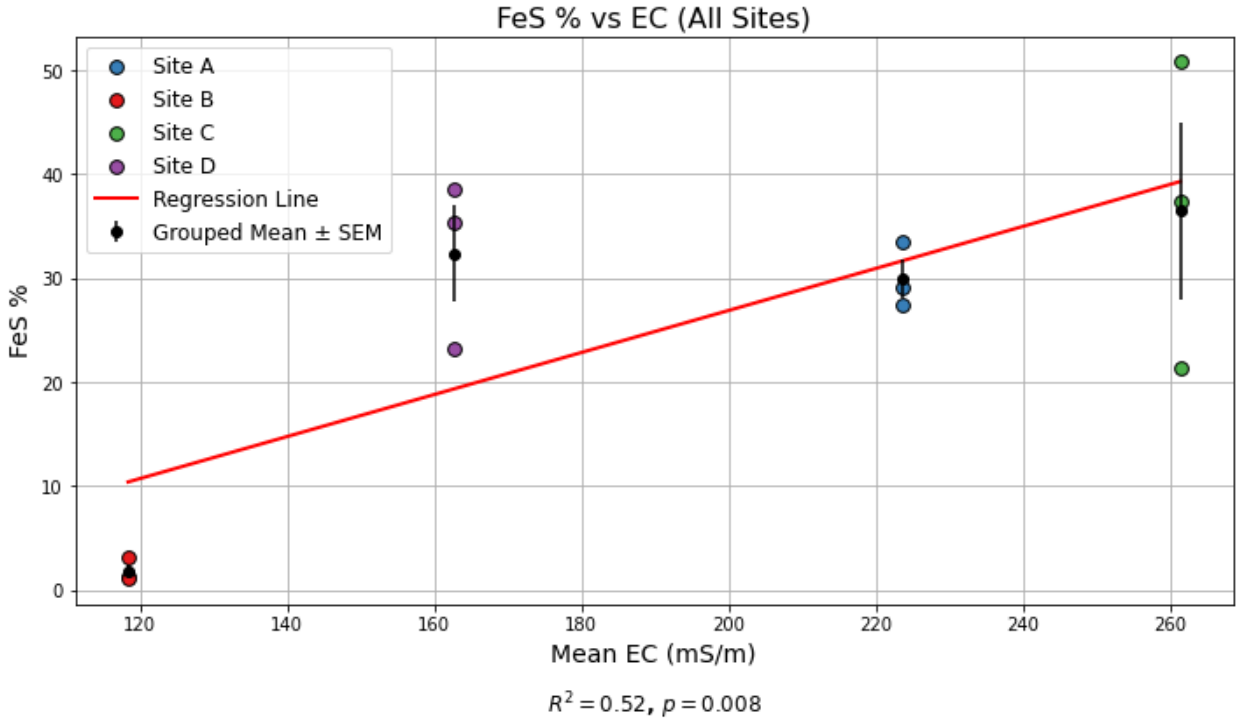

Figure 20: Relationship between mean electrical conductivity (EC) and FeS precipitation across all IRIS deployment sites (A, B, C, and D).

Site	Mean EC ± Std. Dev. (mS/m)	Mean FeS %	Mean FeS Std. Dev. %	Mean FeS SEM %	n
A	223.6 ± 110.9	30.0	3.1	1.8	3.0
B	118.4 ± 35.2	1.9	1.1	0.6	3.0
C	261.4 ± 112.0	36.5	14.7	8.5	3.0

D	162.8 ± 61.6	32.4	8.0	4.6	3.0

Table 5: Summary statistics for mean electrical conductivity (EC) and FeS % coverage across IRIS sites.

The greatest amount of mean FeS % was found at site C, which also had the greatest standard deviation (36.5 ± 14.7%), followed by site D (32.4 ± 8.0%), then site A with 30 ± 3.1%. Lastly, site B had the lowest amount of FeS precipitation with a mean of 1.9 ± 1.1%. A statistically significant and strong positive correlation was observed between EC and FeS content found on the IRIS films ($R = 0.72$, $R^2 = 0.52$, $p = 0.008$). This indicates that approximately half of the variability in FeS content can be explained by variations in EC and provides strong evidence for a relationship between redox conditions and soil conductivity.

3.2.2 FeOOH % vs EC

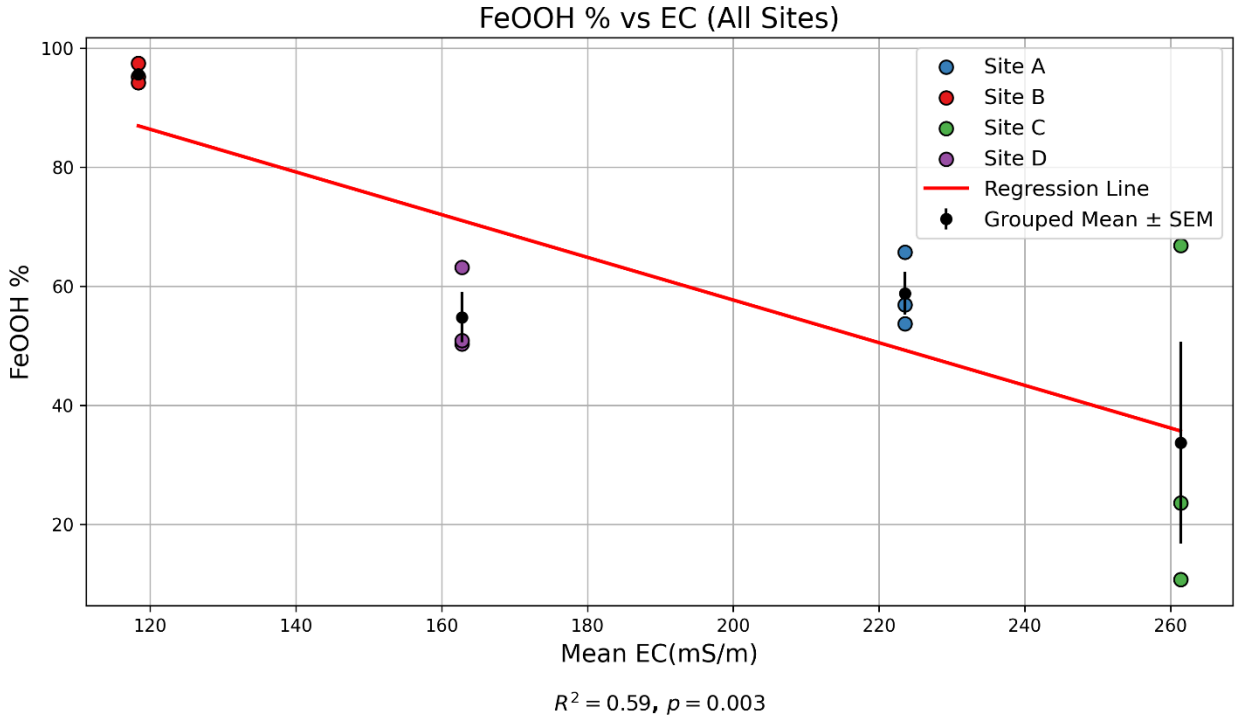

Figure 21: Relationship between mean electrical conductivity (EC) and FeOOH percentage across all IRIS deployment sites (A–D).

Site	Mean EC ± Std. Dev. (mS/m)	Mean FeOOH %	Mean FeOOH Std. Dev. %	Mean FeOOH SEM %	n
A	223.6 ± 110.9	58.7	6.2	3.6	3.0
B	118.4 ± 35.2	95.6	1.7	1.0	3.0
C	261.4 ± 112.0	33.7	29.4	17.0	3.0
D	162.8 ± 61.6	54.8	7.3	4.2	3.0

Table 6: Summary statistics for mean electrical conductivity (EC) and FeOOH % coverage across IRIS sites A–D.

The mean FeOOH percentage decreased as EC values increased. Site B had the lowest mean EC (118.4 ± 35.2 mS/m) and 95.6 ± 1.7% (mean ± std. dev.) FeOOH remaining on the IRIS films, which is the greatest amount that remained between all sites. Site A had the second greatest amount of FeOOH remaining with a significant decrease to 58.7 ± 6.2%, and the second highest mean EC (223.6 ± 110.9 mS/m). Site D had a minimal difference in mean FeOOH (54.8 ± 7.3%) compared to site A, however, the mean EC for site D (162.8 ± 61.6 mS/m) was much lower than A. Site C had the least amount of FeOOH remaining, and the greatest variability (33.7 ± 29.4%).

3.2.3 FeS/Removed Mix % vs EC

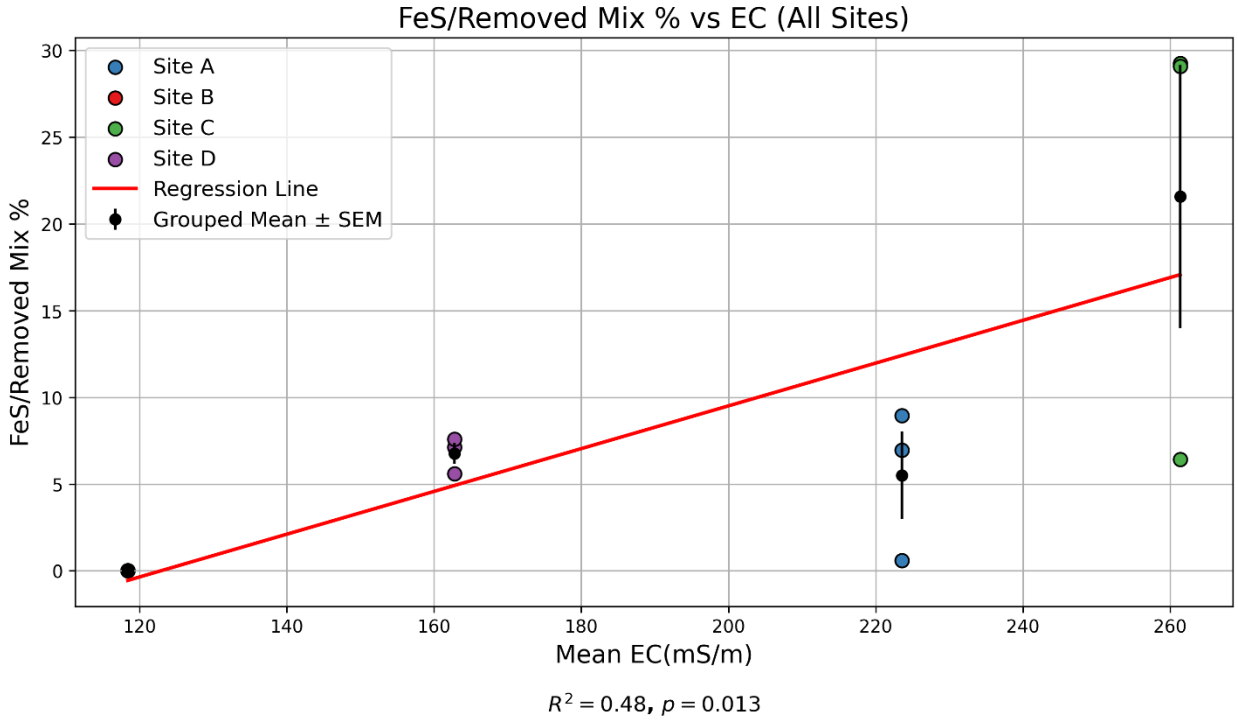

Figure 22: Relationship between mean electrical conductivity (EC) and FeS/Removed Mix percentage across all IRIS deployment sites.

Site	Mean EC ± Std. Dev. (mS/m)	Mean FeS/Removed Mix %	Mean FeS/Removed Mix Std. Dev. %	Mean FeS/Removed Mix SEM %	n
A	223.6 ± 110.9	5.5	4.4	2.5	3.0
B	118.4 ± 35.2	0.0	0.0	0.0	3.0
C	261.4 ± 112.0	21.6	13.1	7.6	3.0
D	162.8 ± 61.6	6.8	1.0	0.6	3.0

Table 7: Summary statistics for mean electrical conductivity (EC) and FeS/Removed Mix % coverage across IRIS sites.

The FeS/Removed Mix % category was the most difficult to classify accurately, as it represents an intermediate redox stage with both FeS precipitation and partial removal. For instance, site C had the largest variation in this category, resulting in a mean ± Std. Dev. of 21.6 ± 13.1%, and an SEM of 7.6%. The variation is much larger than the other sites and can clearly be seen on Figure 22. Site A had the second highest mean and standard deviation (5.5 ± 4.4%), and site D had the smallest standard deviation of 1.0% and a mean of 6.8% FeS/Removed Mix. Site B was found to have no FeS/Removed Mix present. An R^2 value of 0.48 and p-value of 0.013 indicates there is a statistically significant and moderately strong positive correlation between EC and FeS/Removed Mix %. This supports the hypothesis of higher EC values are associated with more active redox zones.

3.2.4 Removed % vs EC

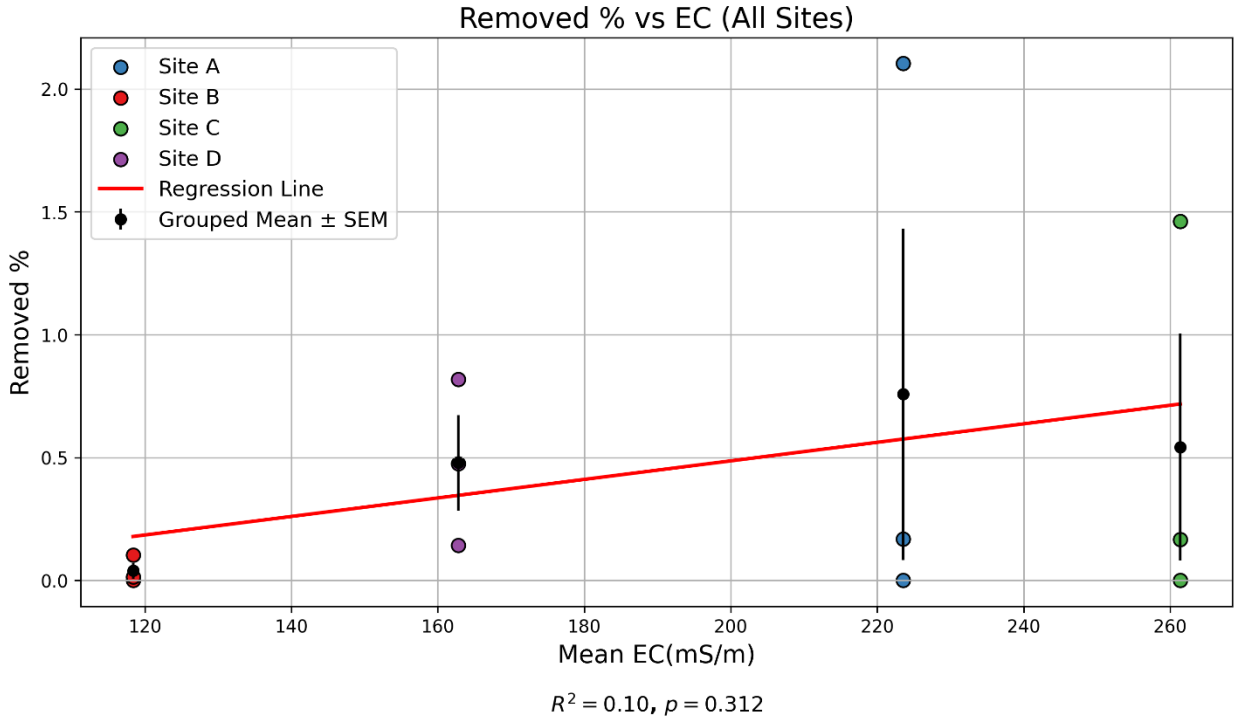

Figure 23: Relationship between mean electrical conductivity (EC) and the percentage of fully removed iron (white film exposure) across all IRIS deployment sites.

Site	Mean EC ± Std. Dev. (mS/m)	Mean Removed %	Mean Removed Std. Dev. %	Mean Removed SEM %	n
A	223.6 ± 110.9	0.8	1.2	0.7	3.0
B	118.4 ± 35.2	0.0	0.1	0.0	3.0
C	261.4 ± 112.0	0.5	0.8	0.5	3.0
D	162.8 ± 61.6	0.5	0.3	0.2	3.0

Table 8: Summary statistics for mean electrical conductivity (EC) and the percentage of "Removed" film (no remaining iron in any phase) across IRIS sites A–D.

The statistical analysis of Removed % in reference to EC increases showed a non-significant correlation ($R^2 = 0.10$, $p = 0.312$) suggesting that EC is not a strong predictor of full iron oxide paint removal. However, it is important to note that there was very limited evidence of full removal at all sites. With less than 3% of total IRIS surface showing complete paint removal for individual points, and the highest Removed % mean ± std. dev. being 0.8 ± 1.2 (Site A), it is likely that the poor correlation is due to insufficient data rather than a lack of relationship. This is further supported by site B having a mean of 0.0 ± 0.1%.

3.3 Discussion

This study investigated the relationship between soil electrical conductivity (EC) and redox potential by correlating electromagnetic induction (EMI) measurements with quantified Indicators of Reduction in Soil (IRIS) data within a sulfur rich environment. Higher EC values aligned with increased iron transformations on IRIS devices, reinforcing the link between redox activity and electrical properties.

The highest EC values for sites A and C were observed at 0.4m and at 0.6m for site D, indicating a redox transition zone between 0.4-0.6m. Site B's maximum EC occurred at 1.6m depth which could imply the redox interface at that location may be deeper than the other sites. Site B is slightly more elevated relative to the other sites which could contribute to a lower water table and influence the degree of redox reactions occurring. It is suspected that EC and redox activity at Zodletone Spring are primarily influenced by the water table. Due to the spring water containing a high concentration of sulfide, redox reactions in the subsurface are likely dependent on spring water interactions. Thus, areas with a potentially lower water table, such as IRIS site B, will not be as reactive while areas that are visibly more saturated towards the surface such as site C, will show evidence of more redox activity on the IRIS films.

Site C experienced an overall maximum EC of 458.7 ± 11.0 mS/m within the redox transition zone and had the greatest amount of FeS precipitation among all sites with 50.79% area coverage after 6 hours. In contrast, site B had a much lower EC peak within the redox transition zone (106.5 ± 27.4 mS/m at 0.4m) and showed only 3.15% FeS coverage after 6 hours. Ultimately, a positive and statistically significant relationship between FeS precipitation and EC was observed ($R^2 = 0.52$, $p = 0.008$), suggesting that half of the FeS accumulation can be explained by variations in EC.

To better assess general trends in FeS precipitation over time, a cumulative regression analysis was performed using grouped mean values for each deployment duration. This approach provides insight into patterns that may not be apparent during individual site analyses. A strong positive relationship ($R^2 = 0.92$) was observed between FeS precipitation and IRIS deployment time, although it was not statistically significant ($p = 0.180$). SEM values increased from 7.8 to 10.0 between 1 to 6 hours, indicating that FeS coverage became more variable over time. While

the cumulative trend suggests a consistent upward trend in FeS precipitation with time, individual observations showed moderate variability and reflect small scale heterogeneity in redox conditions.

These cumulative findings align with individual site trends. Site A showed the strongest correlation between FeS and time ($R^2 = 0.98$, $p = 0.083$), followed closely by site C ($R^2 = 0.97$, $p = 0.104$) and site D ($R^2 = 0.96$, $p = 0.132$), while site B showed a weaker association ($R^2 = 0.77$, $p = 0.319$). Though none of the relationships reached significance thresholds, the consistently high R^2 values across multiple sites support the interpretation that deployment duration has a measurable influence on FeS precipitation.

FeOOH changes from the cumulative analysis showed a weaker temporal relationship ($R^2 = 0.71$, $p = 0.359$) and increasing SEM values from 9.9 to 17.2, indicating greater dispersion around the mean and less consistent behavior compared to FeS. Individual site regressions also exhibit relatively high R^2 values and suggest some degree of time related change with respect to FeOOH, although none of the trends were statistically significant. In contrast, a moderately strong and statistically significant negative relationship was observed between FeOOH and EC ($R^2 = 0.59$, $p = 0.003$), suggesting that FeOOH removal is more strongly associated with subsurface conductivity patterns than deployment duration.

The FeS/Removed Mix category demonstrated a moderate cumulative correlation ($R^2 = 0.64$, $p = 0.410$) with low SEM values, suggesting limited variability in the mean values despite the weaker temporal fit. Site specific regressions for this phase displayed inconsistent trends with poor R^2 and nonsignificant p-values across all locations. However, a moderate and statistically significant correlation was observed between FeS/Removed Mix and EC ($R^2 = 0.48$, $p = 0.013$), implying that the mixed phase could be more influenced by EC rather than time.

In contrast, the Removed phase had the strongest cumulative temporal fit ($R^2 = 0.98$) and lowest p-value ($p = 0.082$), accompanied by minimal variability. This suggests that the full removal of FeOOH is more consistent and has a predictable response over time. Site specific patterns were mixed, as strong fits were observed for sites A and C, but site D showed no significant relationship, and data was insufficient for site B. Additionally, the removed phase had a very weak and nonsignificant relationship with EC ($R^2 = 0.10$, $p = 0.312$), further supporting the idea that full removal may be more time dependent rather than influenced by conductivity. These findings imply that while full removal responds predictably over time, spatial heterogeneity likely limits consistent iron oxide removal across all sites.

It is worth mentioning that full removal of the iron oxide paint from the IRIS films occurred significantly less than FeS precipitation across all locations and durations. These findings are in agreeance with previous research that showed FeS precipitation occurs at a much faster rate than Fe reduction in sulfide rich environments (Duball et al., 2022). Site A had the greatest amount of full FeOOH removal (2.1%) after 6 hours, but FeS precipitation was more dominant at 33.44%. Additionally, site C reached a maximum FeS precipitation of 50.79% and 29.07% FeS/Removed Mix area coverage, while only experiencing 1.46% fully removed FeOOH. Since the formation of FeS is restricted by sulfate reduction, the precipitation of FeS can serve as confirmation that redox potential has decreased beyond Fe reduction and implies a very strongly reduced and anaerobic environment (Duball et al., 2020).

These results have practical implications for wetland scientists and biogeochemists studying sulfur and iron redox cycling in sulfidic environments. FeS formation is often tied to microbial sulfate reduction, which regulates nutrient availability, trace metal mobility, and greenhouse gas emissions in wetland systems (Fiedler et al., 2007; Schröder et al., 2016). By identifying active

redox zones through EMI surveying methods, researchers can infer microbial activity, track biogeochemical changes, and evaluate restoration without relying on invasive sampling techniques which are more labor intensive and spatially limited.

3.3.1 Limitations

Despite the strength of the observed correlations between EC and iron redox transformations, several limitations should be acknowledged. For example, EMI inversion accuracy is often reduced at the shallowest and deepest depths due to boundary effects that limit coil sensitivity, potentially impacting interpretations at 0m and 2.3m. Additionally, while IRIS films provide direct evidence of redox activity over a fixed duration, film strips may not uncurl completely during deployment, resulting in some regions not being in full contact with the soil. In turn, this would significantly affect the area % of each category.

Furthermore, EC is influenced by several factors beyond redox potential, including salinity, soil texture, grain mineralogy, temperature, moisture content, and ion mobility (Corwin & Lesch, 2005; Doolittle & Brevik, 2014; McNeill, 1980a). As a result, disentangling redox related EC changes from other contributing factors can be challenging in heterogeneous and complex soil profiles. Due to a lack of published studies that integrate EMI and IRIS methods, there is considerable uncertainty regarding if and when they should be used in tandem.

Hodges et al. (2019) is one of the only published studies to integrate EMI and in situ redox indicators. The study did not find a consistent or strong relationship between EMI measurements and Fe reduction; however, it does highlight that heterogeneity in water and clay distribution can complicate the interpretation when using EMI data as a proxy for redox potential. This aligns with previous research that suggests EMI methods are most successful at predicting soil

properties when there is only one dominate factor affecting measurements (Doolittle & Collins, 1998; McNeill, 1980a). Ultimately, although EMI and IRIS integration offers a robust framework for redox mapping, the method's transferability to environments with different soil textures and hydrological activity may require adaptation.

3.3.2 Implications

This study was conducted in the context of acid sulfate soils, which can pose serious environmental threats when oxidized. Disturbance of these soils, often during wetland drainage for urbanization or agriculture, can result in the formation of sulfuric acid, leading to vegetation degradation, fish habitat loss, and long-term environmental deterioration (Berkowitz et al., 2019; Dent & Pons, 1995; Wessel & Rabenhorst, 2017). By using EMI and IRIS devices to detect active redox zones and interfaces, this study provides a foundation for noninvasive monitoring acid sulfate soil formation and support wetland protection and remediation efforts. EMI based approaches can help identify at risk areas before oxidation occurs, aiding in land management for mitigating harmful consequences through targeted hydrological restoration.

The variation in peak EC depths across the IRIS sites highlights the role local hydrology and geochemical conditions play in determining the spatial distribution of redox activity. Site B's lower EC and minimal Fe transformations may reflect more oxidized and less saturated conditions, which would influence differences in organic carbon and possibly mineralogical structure (Wessel & Rabenhorst, 2017). This calls attention to the importance of site-specific factors in governing redox dynamics and reinforces the value of integrating EMI with IRIS devices in future soil studies.

In addition to Earth based applications, these findings also inform planetary science, particularly the search for biosignatures and redox gradients on Mars. Both iron sulfides and iron oxides have been detected in Martian sediments and are considered indicative of past redox cycling (Wong et al., 2021). By establishing a correlation between FeS accumulation and EC in a terrestrial analog environment, this study supports the usefulness of EMI based instruments on future Mars missions. Such tools could help identify redox active zones, prioritize subsurface targets for life detection, and enhance habitability assessments in sulfur rich environments.

3.3.3 Future Directions

Building on the results of this study, several steps could improve the interpretation of redox processes in sulfur rich environments. Groundwater sampling would allow for a direct measurement of geochemical parameters such as pH, sulfide concentrations, and dissolved oxygen, providing a chemical context for interpreting iron phase transformation. Seasonal deployments of IRIS devices and concurrent EMI surveys could reveal temporal patterns in redox activity at Zodletone Spring, offering insights to how water table fluctuations and climate variability affect subsurface conditions. Additionally, calibrating ERT survey data with EMI transects could improve the confidence of true conductivity values and overall improve interpretations of geophysical surveys. Measuring salt concentrations and total dissolved solids would also help distinguish the degree of salinity induced EC variations, which would be particularly relevant in coastal or estuarine systems. Finally, piezometric sensors have been installed to begin monitoring groundwater level fluctuations, however additional data collection is required before a groundwater model can be developed. Once sufficient data is available, integrating EMI, ERT, and piezometric datasets will provide insight into hydrological influences on redox zones and aid in predicting subsurface reactivity.

Bibliography

Apalara, I. T., Hodges, C., Sabisch, J. E. C., Elwood Madden, M. E., Larson, P. R., & Elwood Madden, A. S. (2025). Understanding the Impact of a Modern Euxinic Spring on Sediment Using Bulk Sediment and Smectite Clay-Preserved Proxies. *ACS Earth and Space Chemistry*, *9*(2), 265–276. https://doi.org/10.1021/acsearthspacechem.4c00269

Atekwana, E. A., & Slater, L. D. (2009). Biogeophysics: A new frontier in Earth science research. *Reviews of Geophysics*, *47*(4). https://doi.org/10.1029/2009RG000285

Bachman, E. E., Hullaster, D., Krumholz, L. R., & Elwood Madden, A. S. (2018, November 6). *BIOTIC AND ABIOTIC MINERALOGICAL SIGNATURES INDUCED BY EUXINIC METHANE-RICH BRINE SPRING DISCHARGE*. GSA Annual Meeting in Indianapolis, Indiana, USA - 2018. https://gsa.confex.com/gsa/2018AM/webprogram/Paper324175.html

Berkowitz, J. F., VanZomeren, C. M., & Fresard, N. D. (2019). Rapid formation of iron sulfides alters soil morphology and chemistry following simulated marsh restoration. *Geoderma*, *351*, 76–84. https://doi.org/10.1016/j.geoderma.2019.05.028

Berkowitz, J. F., Vepraskas, M. J., Vaughan, K. L., & Vasilas, L. M. (2021). Development and application of the Hydric Soil Technical Standard. *Soil Science Society of America Journal*, *85*(3), 469–487. https://doi.org/10.1002/saj2.20202

Camprubi, E., Jordan, S. F., Vasiliadou, R., & Lane, N. (2017). Iron catalysis at the origin of life. *IUBMB Life*, *69*(6), 373–381. https://doi.org/10.1002/iub.1632

Castenson, K. L., & Rabenhorst, M. C. (2006). Indicator of Reduction in Soil (IRIS): Evaluation of a New Approach for Assessing Reduced Conditions in Soil. *Soil Science Society of America Journal*, *70*(4), 1222–1226. https://doi.org/10.2136/sssaj2005.0130

Clément, R., Pärn, J., Maddison, M., Henine, H., Chaumont, C., Tournebize, J., Uri, V., Espenberg, M., Günther, T., & Mander, Ü. (2020). Frequency-domain electromagnetic induction for upscaling greenhouse gas fluxes in two hemiboreal drained peatland forests. *Journal of Applied Geophysics*, *173*, 103944. https://doi.org/10.1016/j.jappgeo.2020.103944

Corwin, D. L., & Lesch, S. M. (2005). Apparent soil electrical conductivity measurements in agriculture. *Computers and Electronics in Agriculture*, *46*(1), 11–43. https://doi.org/10.1016/j.compag.2004.10.005

Corwin, D. L., & Rhoades, J. (1982). An Improved Technique for Determining Soil Electrical Conductivity-Depth Relations from Above-ground Electromagnetic Measurements1. *Soil Science Society of America Journal - SSSAJ*, *46*. https://doi.org/10.2136/sssaj1982.03615995004600030014x

Corwin, D. L., & Rhoades, J. D. (1984). Measurement of Inverted Electrical Conductivity Profiles Using Electromagnetic Induction. *Soil Science Society of America Journal*, *48*(2), 288–291. https://doi.org/10.2136/sssaj1984.03615995004800020011x

Coscia, I., Greenhalgh, S. A., Linde, N., Doetsch, J., Marescot, L., Günther, T., Vogt, T., & Green, A. G. (2011). 3D crosshole ERT for aquifer characterization and monitoring of infiltrating river water. *GEOPHYSICS*, *76*(2), G49–G59. https://doi.org/10.1190/1.3553003

Darmody, R. G., Fanning, D. S., Drummond Jr., W. J., & Foss, J. E. (1977). Determination of Total Sulfur in Tidal Marsh Soils by X-ray Spectroscopy. *Soil Science Society of America Journal*, *41*(4), 761–765. https://doi.org/10.2136/sssaj1977.03615995004100040030x

1183 Dent, D. L., & Pons, L. J. (1995). A world perspective on acid sulphate soils. *Geoderma*, *67*(3–
1184 4), 263–276. https://doi.org/10.1016/0016-7061(95)00013-E
1185 Donovan, R. N., & Ditzler, C. (1986). Stop 3: Geologic highlights at Zodletone (Stinking
1186 Mountain). In *Geology of The Eastern Wichita Mountains Southwestern Oklahoma* (pp.
1187 96–99). Oklahoma Geological Survey.
1188 Doolittle, J. A., & Brevik, E. C. (2014). The use of electromagnetic induction techniques in soils
1189 studies. *Geoderma*, *223–225*, 33–45. https://doi.org/10.1016/j.geoderma.2014.01.027
1190 Doolittle, J. A., & Collins, M. E. (1998). A comparison of EM induction and GPR methods in
1191 areas of karst. *Geoderma*, *85*(1), 83–102. https://doi.org/10.1016/s0016-7061(98)00012-3
1192 Duball, C., Andersen, M. L., Beaudette, D., & Vaughan, K. L. (2022). *Rapid formation of iron*
1193 *monosulfide on Indicator of Reduction in Soil devices in S-rich hydric soils—Duball—*
1194 *2023—Soil Science Society of America Journal—Wiley Online Library*.
1195 https://acsess.onlinelibrary.wiley.com/doi/abs/10.1002/saj2.20511
1196 Duball, C., Vaughan, K., Berkowitz, J. F., Rabenhorst, M. C., & VanZomeren, C. M. (2020). Iron
1197 monosulfide identification: Field techniques to provide evidence of reducing conditions
1198 in soils. *Soil Science Society of America Journal*, *84*(2), 303–313.
1199 https://doi.org/10.1002/saj2.20044
1200 Fanning, D. S., Rabenhorst, M. C., & Fitzpatrick, R. W. (2017). Historical developments in the
1201 understanding of acid sulfate soils. *Geoderma*, *308*, 191–206.
1202 https://doi.org/10.1016/j.geoderma.2017.07.006
1203 Fanning, D. S., Rabenhorst, M. C., May, L., & Wagner, D. P. (1989). Oxidation State of Iron in
1204 Glauconite from Oxidized and Reduced Zones of Soil-Geologic Columns. *Clays and*
1205 *Clay Minerals*, *37*(1), 59–64. https://doi.org/10.1346/CCMN.1989.0370107

Fiedler, S., Vepraskas, M., & Richardson, J. (2007). Soil redox potential: Importance, field measurements, and observations. *Advances in Agronomy*, *94*. https://app.readcube.com/library/4ad735b9-ab4a-4781-8b0e-b8aee7a82081/item/8a5e3d47-ec79-4712-b18d-ccc606377eb0

Hall, S. J., Liptzin, D., Buss, H. L., DeAngelis, K., & Silver, W. L. (2016). Drivers and patterns of iron redox cycling from surface to bedrock in a deep tropical forest soil: A new conceptual model. *Biogeochemistry*, *130*(1–2), 177–190. https://doi.org/10.1007/s10533-016-0251-3

Hodges, C., Mallard, J., Markewitz, D., Barcellos, D., & Thompson, A. (2019). Seasonal and spatial variation in the potential for iron reduction in soils of the Southeastern Piedmont of the US. *CATENA*, *180*, 32–40. https://doi.org/10.1016/j.catena.2019.03.026

Husson, O. (2013). *Redox potential (Eh) and pH as drivers of soil/plant/microorganism systems: A transdisciplinary overview pointing to integrative opportunities for agronomy*. https://doi.org/10.1007/s11104-012-1429-7

Jenkinson, B., & Franzmeier, D. (2006). Development and Evaluation of Iron-Coated Tubes that Indicate Reduction in Soils. *Soil Science Society of America Journal - SSSAJ*, *70*. https://doi.org/10.2136/sssaj2004.0323

Johnston, D. T., Wolfe-Simon, F., Pearson, A., & Knoll, A. H. (2009). Anoxygenic photosynthesis modulated Proterozoic oxygen and sustained Earth's middle age. *Proceedings of the National Academy of Sciences*, *106*(40), 16925–16929. https://doi.org/10.1073/pnas.0909248106

Kölbl, A., Marschner, P., Fitzpatrick, R., Mosley, L., & Kögel-Knabner, I. (2017). Linking organic matter composition in acid sulfate soils to pH recovery after re-submerging. *Geoderma*, *308*, 350–362. https://doi.org/10.1016/j.geoderma.2017.07.031

Lindsay, W. L. (1979). *Chemical equilibria in soils.* John Wiley and Sons Ltd.

McAdam, A. C., Sutter, B., Archer, P. D., Franz, H. B., Wong, G. M., Lewis, J. M. T., Clark, J. V., Millan, M., Williams, A. J., Eigenbrode, J. L., Knudson, C. A., Freissinet, C., Glavin, D. P., Stern, J. C., Navarro-González, R., Achilles, C. N., Ming, D. W., Morris, R. V., Bristow, T. F., … Malespin, C. A. (2022). Evolved Gas Analyses of Sedimentary Rocks From the Glen Torridon Clay-Bearing Unit, Gale Crater, Mars: Results From the Mars Science Laboratory Sample Analysis at Mars Instrument Suite. *Journal of Geophysical Research: Planets*, *127*(9), e2022JE007179. https://doi.org/10.1029/2022JE007179

McLachlan, P., Blanchy, G., & Binley, A. (2021). EMagPy: Open-source standalone software for processing, forward modeling and inversion of electromagnetic induction data. *Computers & Geosciences*, *146*, 104561. https://doi.org/10.1016/j.cageo.2020.104561

McLachlan, P., Blanchy, G., Chambers, J., Sorensen, J., Uhlemann, S., Wilkinson, P., & Binley, A. (2021). The Application of Electromagnetic Induction Methods to Reveal the Hydrogeological Structure of a Riparian Wetland. *Water Resources Research*, *57*(6). https://doi.org/10.1029/2020wr029221

McNeill, J. D. (1980a). *Electrical Conductivity of Soils and Rocks* (Technical Note No. TN-5). Geonics Limited.

McNeill, J. D. (1980b). *Electromagnetic Terrain Conductivity Measurement at Low Induction Numbers* (Techincal Note No. TN-6). Geonics Limited.

1249 Mebel, A. M., & Hwang, D.-Y. (2001). Theoretical Study of the Reaction Mechanism of Fe
1250 Atoms with H2O, H2S, O2 and H+. *The Journal of Physical Chemistry A*, *105*(31),
1251 7460–7467. https://doi.org/10.1021/jp011324s
1252 Miller, C. R., Routh, P. S., Brosten, T. R., & McNamara, J. P. (2008). Application of time-lapse
1253 ERT imaging to watershed characterization. *Geophysics*, *73*(3), G7–G17.
1254 https://doi.org/10.1190/1.2907156
1255 Pathirana, S., Lambot, S., Krishnapillai, M., Cheema, M., Smeaton, C., & Galagedara, L. (2023).
1256 Ground-Penetrating Radar and Electromagnetic Induction: Challenges and Opportunities
1257 in Agriculture. *Remote Sensing*, *15*(11), Article 11. https://doi.org/10.3390/rs15112932
1258 Pons, L. J. (1973). Outline of the genesis, characteristics, classification and improvement of acid
1259 sulphate soils. In H. Dost (Ed.), *Proceedings of the 1st International Symposium on Acid*
1260 *Sulphate Soils, 13–20 August 1972* (pp. 3–27). International Institute for Land
1261 Reclamation and Improvement.
1262 Rabenhorst, M. C., & Burch, S. N. (2006). Synthetic Iron Oxides as an Indicator of Reduction in
1263 Soils (IRIS). *Soil Science Society of America Journal*, *70*(4), 1227–1236.
1264 https://doi.org/10.2136/sssaj2005.0354
1265 Rabenhorst, M. C., & Hively, W. (2009). Measurements of soil redox potential. *Soil Science*
1266 *Society of America Journal*, *73*. https://app.readcube.com/library/4ad735b9-ab4a-4781-
1267 8b0e-b8aee7a82081/item/24c5dedb-abc2-455a-bc87-99e1aa6c4f31
1268 Rabenhorst, M. C., Megonigal, J., & Keller, J. (2010). Synthetic iron oxides for documenting
1269 sulfide in marsh pore water. *Soil Science Society of America*, *74*.
1270 https://app.readcube.com/library/4ad735b9-ab4a-4781-8b0e-
1271 b8aee7a82081/item/434ddd1b-17c4-4a8f-8170-84f1270817c1

Rampe, E. B., Blake, D. F., Bristow, T. F., Ming, D. W., Vaniman, D. T., Morris, R. V., Achilles, C. N., Chipera, S. J., Morrison, S. M., Tu, V. M., Yen, A. S., Castle, N., Downs, G. W., Downs, R. T., Grotzinger, J. P., Hazen, R. M., Treiman, A. H., Peretyazhko, T. S., Des Marais, D. J., … Wiens, R. C. (2020). Mineralogy and geochemistry of sedimentary rocks and eolian sediments in Gale crater, Mars: A review after six Earth years of exploration with *Curiosity*. *Geochemistry*, *80*(2), 125605. https://doi.org/10.1016/j.chemer.2020.125605

Russel, M. J., Daniel, R. M., Hall, A. J., & Sherringham, J. A. (1994). A hydrothermally precipitated catalytic iron sulphide membrane as a first step toward life. *ResearchGate*. https://doi.org/10.1007/BF00160147

Sanders, W. E. (1998). *Rate and Mechanism of In Situ Barite Precipitation at Zodletone Mountain, Southwestern Oklahoma, USA*. University of Oklahoma.

Sapkota, Y., Duball, C., Vaughan, K., Rabenhorst, M. C., & Berkowitz, J. F. (2022). Indicator of Reduction in Soil (IRIS) devices: A review. *Science of The Total Environment*, *852*, 158419. https://doi.org/10.1016/j.scitotenv.2022.158419

Schröder, C., Köhler, I., Muller, F. L. L., Chumakov, A. I., Kupenko, I., Rüffer, R., & Kappler, A. (2016). The biogeochemical iron cycle and astrobiology. *Hyperfine Interactions*, *237*(1), 85. https://doi.org/10.1007/s10751-016-1289-2

Schwertmann, U., & Taylor, R. m. (1989). Iron Oxides. In *Minerals in Soil Environments* (pp. 379–438). John Wiley & Sons, Ltd. https://doi.org/10.2136/sssabookser1.2ed.c8

Senko, J. M., Campbell, B. S., Henriksen, J. R., Elshahed, M. S., Dewers, T. A., & Krumholz, L. R. (2004). Barite deposition resulting from phototrophic sulfide-oxidizing bacterial

activity. *Geochimica et Cosmochimica Acta*, *68*(4), 773–780. https://doi.org/10.1016/j.gca.2003.07.008

Toushmalani, R. (2010). Application of geophysical methods in agriculture. *Australian Journal of Basic and Applied Sciences*, *4*, 6433–6439.

USDA-NRCS. (2024). *Field Indicators of Hydric Soils in the United States*. *Version 9.0*. https://www.nrcs.usda.gov/sites/default/files/2024-09/Field-Indicators-of-Hydric-Soils.pdf

Van De Vijver, E., Van Meirvenne, M., Saey, T., Delefortrie, S., De Smedt, P., De Pue, J., & Seuntjens, P. (2015). Combining multi-receiver electromagnetic induction and stepped frequency ground penetrating radar for industrial site investigation. *European Journal of Soil Science*, *66*(4), 688–698. https://doi.org/10.1111/ejss.12229

Vaughan, K. L., Miller, F., Navarro, N., & Appel, C. (2016). Visual Assessment of Sulfate Reduction to Identify Hydric Soils. *Soil Science Society of America Journal*, *80*(4), 1114–1119. https://doi.org/10.2136/sssaj2016.02.0035

Wächtershäuser, G. (1992). Groundworks for an evolutionary biochemistry: The iron-sulphur world. *Progress in Biophysics and Molecular Biology*, *58*(2), 85–201. https://doi.org/10.1016/0079-6107(92)90022-X

Wessel, B. M., & Rabenhorst, M. C. (2017). Identification of sulfidic materials in the Rhode River subestuary of Chesapeake Bay. *Geoderma*, *308*, 215–225. https://doi.org/10.1016/j.geoderma.2017.07.025

Wong, G. M., Franz, H. B., Clark, J. V., Mcadam, A. C., Lewis, J. M. T., Millan, M., Ming, D. W., Gomez, F., Clark, B., Eigenbrode, J., Navarro-González, R., & House, C. H. (2021). Oxidized and reduced sulfur observed by the Sample Analysis at Mars (SAM) instrument

suite on the Curiosity rover within the Glen Torridon region at Gale crater, Mars. *Journal of Geophysical Research. Planets*, *6*(1), 129–140. https://doi.org/10.1029/2021je007084

Yao, W., & Millero, F. J. (1996). Oxidation of hydrogen sulfide by hydrous Fe(III) oxides in seawater. *Marine Chemistry*, *52*(1), 1–16. https://doi.org/10.1016/0304-4203(95)00072-0

Younger, P. L. (1984). *Barite Travertine from Southwestern Oklahoma and West—Central Colorado*. Oklahoma State Univeristy.

Zhang, Z., & Furman, A. (2021). Soil redox dynamics under dynamic hydrologic regimes—A review. *Science of The Total Environment*, *763*, 143026. https://doi.org/10.1016/j.scitotenv.2020.143026